CHAPTER 1

Introduction

Convective downdrafts have long been recognized as important features of thunderstorm circulations. As early as the turn of the century, scientists noticed strong winds associated with rain showers (Humphreys, 1914), but the mechanisms behind downdraft formation were not understood until the last few decades. With the advent of new technology, including fast computer processors and Doppler radar, meteorologists have been able to study downdrafts within thunderstorms with much more detail. Numerical models have been created to simulate downdraft dynamics, and observations with instruments mounted on airplanes have become much more common.

By definition, downdrafts are nothing more than areas of downward moving air. Their scale and intensity can vary, so subclassifications have been created to more accurately describe the descending air. Mesoscale downdrafts are often associated with mesoscale convective systems, and have horizontal scales on the order of 10-100 km. Convective

downdrafts are smaller and often more intense than the mesoscale variety. They are anywhere from tens of meters to several kilometers in diameter, and can reach downward vertical velocities of 30 ms^{-1}. Fujita and Byers (1977) defined downbursts as particularly strong downdrafts which maintain a strong current (greater than 10 ms^{-1}) near the ground. Fujita and Wakimoto (1983) further divided downbursts into macrobursts and microbursts, having horizontal scales on the order of 10 s of kilometers and 100 s of meters, respectively. During the early 1980 s, Fujita attributed several aircraft accidents to microbursts, and scientific interested blossomed as a result.

Convective downdrafts are driven by cooling due to melting and evaporation of precipitation, condensate loading, and pressure forces. As water droplets or ice crystals fall from a cloud into subsaturated air, some are melted, evaporated, or sublimated. Latent heat is therefore removed from the environment, producing a bubble of air that is cooler than the surrounding air. This negatively buoyant parcel then descends as long as it remains cooler than its environment. Profiles with very steep lapse rates have temperatures which increase rapidly with decreasing height, so downdrafts are easily able to remain cooler than the surrounding air. These environments are therefore most conducive for downdraft development and maintenance, but even conditionally unstable layers can produce intense downdrafts.

Condensate loading also increases downdraft velocities, although the magnitude of this forcing is generally less than evaporation (Knupp and Cotton, 1985). During intense rainfall, fairly large drops can be quite numerous, weighing down the air and causing it to descend. Interestingly, precipitation loading alone can initiate a downdraft in a stable environment. For example, if a parcel of air is saturated and rain falls into it, evaporation

will not occur and the parcel will remain neutrally buoyant. However, the weight of the rain could possibly cause the parcel to descend to a subsaturated layer, where evaporation could commence and its downward velocity would increase. Such a downdraft could continue to accelerate and become very intense at a lower level. For this reason, condensate loading can not be ignored.

Strong locally induced pressure gradients are common in thunderstorms, especially supercells. Low pressure formation near the surface could produce a downward directed pressure gradient force, which could enhance an existing downdraft. Oppositely, high pressure near the surface could offset some negative buoyancy and cause a downdraft to decelerate. Since these local areas of high/low pressure are nearly impossible to measure, they are the least understood factors affecting convective downdrafts, so including their effects in models is very difficult.

With the advent of fast computer processors, numerical models of atmospheric phenomena have become more practical and much more common in recent years. In order to create a working model, the physics behind the physical processes must be understood and governing equations must be developed. Assumptions are almost always necessary, and since they often introduce errors, models also have errors. Convective downdraft models were first developed in the 1960 s and have since been drastically improved. Given an environmental profile of temperature and moisture, models can predict the magnitude and nature of thunderstorm updrafts and downdrafts.

Testing model results with actual data is difficult because measuring winds within thunderstorms is not easy. Aircraft can penetrate into weak storms to obtain temperature and wind information, but the intense updrafts and downdrafts associated with large thun-

derstorms create very dangerous conditions. Doppler radar was first introduced in the 1940 s and the technology has been steadily evolving ever since. With two Doppler radars positioned within 40 or 50 kilometers of each other, radial velocity measurements can be combined to obtain profiles of divergence. Vertical velocity profiles can then be calculated by integrating the continuity equation from the top of the storm downward. Although errors are common, this method allows scientists to study windflow patterns within very intense thunderstorms, including the evolution of updrafts and downdrafts.

This thesis attempts to understand the behavior of convective downdrafts by using a simple model and Doppler radar data. The model is one-dimensional and steady-state, and generates profiles of vertical velocity, water vapor, and rainwater within a downdraft column. Model results are compared to observational Doppler radar data, including dual-Doppler vertical velocity calculations. Conclusions are drawn from sensitivity tests of the model alone, by examination of the radar data, and finally by using radar results to initialize the model and compare with actual observations.

Chapter 2 discusses previous work with convective downdrafts and Doppler radar. Chapter 3 introduces the model by providing equations and discretization methods, and gives results from model sensitivity tests. Chapter 4 introduces the radar case studies by providing dual-Doppler results and downdraft analysis using model data only. Chapter 5 combines the radar results with model runs to test the model s performance, as well as to understand convective downdraft structure and evolution. Finally, Chapter 6 provides conclusions and suggestions for future work.

CHAPTER 2

Scientific Background

2.1 Introduction

The kinematic and thermodynamic structure of thunderstorms has been studied since the first part of the nineteenth century. Early studies relied almost entirely on human observations of thunderstorm behavior. Later, ground measurements allowed scientists to examine temperature and wind fields in the inflow and outflow portions of storms, which lead to speculation about the existence and nature of updrafts and downdrafts. Not until the introduction of Doppler radar were researchers able to obtain accurate measurements of updraft and downdraft velocities. Despite advances in radar and other observing technologies, downdraft kinematics and thermodynamics are still not completely understood. This chapter briefly summarizes previous authors work in thunderstorm downdrafts and Doppler radar observations.

2.2 Convective Downdrafts

Convective downdrafts were observed and documented in the early 1900 s, although the authors certainly did not understand the details of the mechanisms behind their formation. Humphreys (1914) noticed strong surface winds in the vicinity of rain shafts, and suggested that downdrafts formed as the falling precipitation evaporated. The downward moving air then spread outward as it reached the surface and produced gusty winds.

Byers and Braham (1949), using data collected during the Thunderstorm Project, concluded that convective-scale downdrafts were important features of cloud circulations. They documented the existence of downdrafts with magnitudes approaching 20 ms^{-1}; maximum vertical velocities values were suggested to occur at mid-levels. Entrainment within the updraft and precipitation loading were hypothesized to be the primary forcing mechanisms. They also suggested that updraft overshooting and subsequent descent could be responsible for downdraft development. Even though the detailed kinematic structure of downdrafts was not presented, this pioneering work set the stage for future studies of convective downdrafts.

Betts (1976) created a simple two-layer model to study the effects of downdrafts on the sub-cloud layer. Air within this sub-cloud layer rises in updrafts, and is replaced by downdraft air from the layer above (Figure 2.1). As the storm advances (toward the left in the figure), boundary layer air is lifted into the updraft, and air within the cloud descends downward, forming a gust front which propagates with the storm. The new thermodynamic quantities can then be calculated for both layers, and the result is cooler air in the

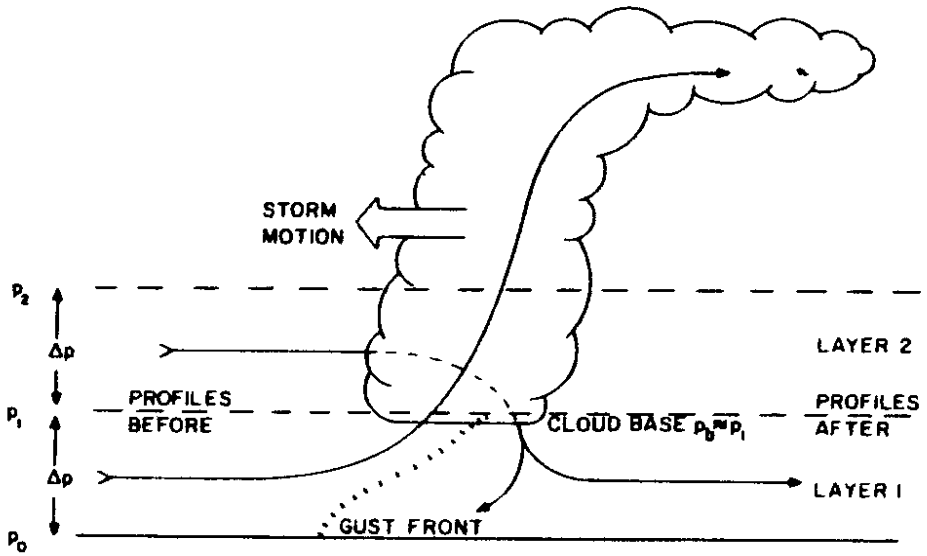


FIGURE 2.1:> Schematic airflow relative to travelling mesosystem, showing two-layer model exchange: inflow layer p_2 to p_1 ascends in updrafts and inflow layer p_1 to p_2 descends in downdrafts in replacements. (Actual flow inside system will be both three-dimensional and transient, not two-dimensional as sketched.) From Betts (1976).

boundary layer. This model does not attempt to resolve the detailed kinematics and dynamics associated with the updraft and downdraft circulations.

Attempts were made in the 1970 s to model the total cumulus fluxes of mass, heat, and moisture on the synoptic scale. Arakawa and Schubert (1974) developed a cumulus parameterization which allowed subcloud air to be transported upwards in cumulus updrafts. However, downdraft mass transport was neglected, so the boundary layer ended up too warm and dry. Johnson (1976) developed a diagnostic model in order to estimate the contribution of convective-scale downdrafts to synoptic scale cumulus fluxes. Each updraft was assumed to have a corresponding downdraft which entrained the same environmental air, and the entrainment rate was assumed to be the same for both updrafts and downdrafts. The downdraft was modeled as an inverted plume and was driven by precipitation drag and evaporation. (Figure 2.2)

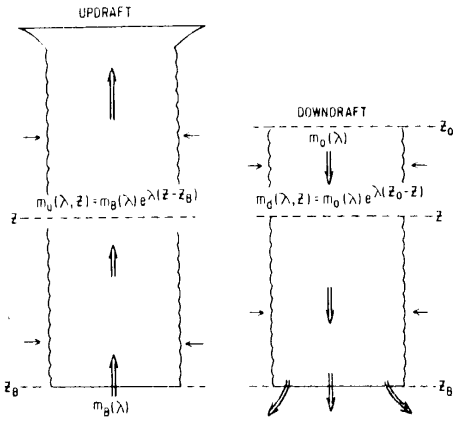


FIGURE 2.2:> Model for updraft and downdraft of cloud type λ. Units of $m_B(\lambda)$ and $m_O(\lambda)$ are $mbkmday^{-1}$. From Johnson (1976).

The updraft and downdraft were assumed to be separate, so that interactions between them could be neglected. However, the downdraft was supplied with precipitation which was generated in the updraft, allowing the downdraft to be negatively buoyant from precipitation loading and evaporation. After testing the model with two different data sets, Johnson concluded that the inclusion of downdrafts allowed cool, moist air to reach the lower troposphere, offsetting the warm bias observed by previous authors.

Downdrafts within cumulonimbus clouds can be very powerful, causing damage both to aircraft and surface structures. Fujita and Byers (1977) examined satellite and radar data from 24 June 1975 near New York s JFK airport in order to explain the crash of an airliner. The plane was trying to land during a thundershower, but crashed short of the runway. Fujita attributed the accident to a downburst, an unusually strong downdraft occurring within a thunderstorm. Vertical velocities within downbursts can reach greater than 30 ms^{-1}, much higher than values estimated from the Thunderstorm Project in 1946

and 1947. These violent downdrafts strike the surface and spread outward, producing very strong straight-line winds than can level homes and other structures.

Knupp and Cotton (1985) presented an interpretive survey of convective downdrafts using observational data and modeling results. (Figure 2.3) is a schematic of a typical thunderstorm containing updrafts, downdrafts, and entrainment. The area labeled PR is a precipitation associated downdraft which results from precipitation falling from the tilted updraft into subsaturated air and evaporating. As the air cools and descends, it strikes the surface and surges horizontally as a gust front. Knupp and Cotton concluded that convective downdraft structure is highly dependent on static stability of the environment, wind shear profiles, cloud microphysical processes, and precipitation characteristics. Vertical velocity magnitudes are typically 5-10 ms^{-1} within downdrafts, but can reach 20 ms^{-1}. Additionally, precipitating downdrafts descend to the surface from heights of near cloud base up to ~5 *km*, and can have horizontal scales similar to the low-level precipitation regions beneath cumulonimbus clouds.

Srivastava (1985) presented a one-dimensional, time-dependent model of an evaporatively driven downdraft in order to study microbursts. The model predicted raindrop evaporation, raindrop concentration, water substance, thermodynamic energy, and vertical velocity. Evaporation was calculated based on the size distribution, and the corresponding decrease in downdraft temperature could be obtained. Entrainment into the downdraft column was represented as an inflow velocity proportional to the difference between vertical velocities of the column and its environment. The author acknowledged that this highly simplified treatment of entrainment is quite uncertain since the mechanisms were not understood. After running the model under a variety of atmospheric conditions,

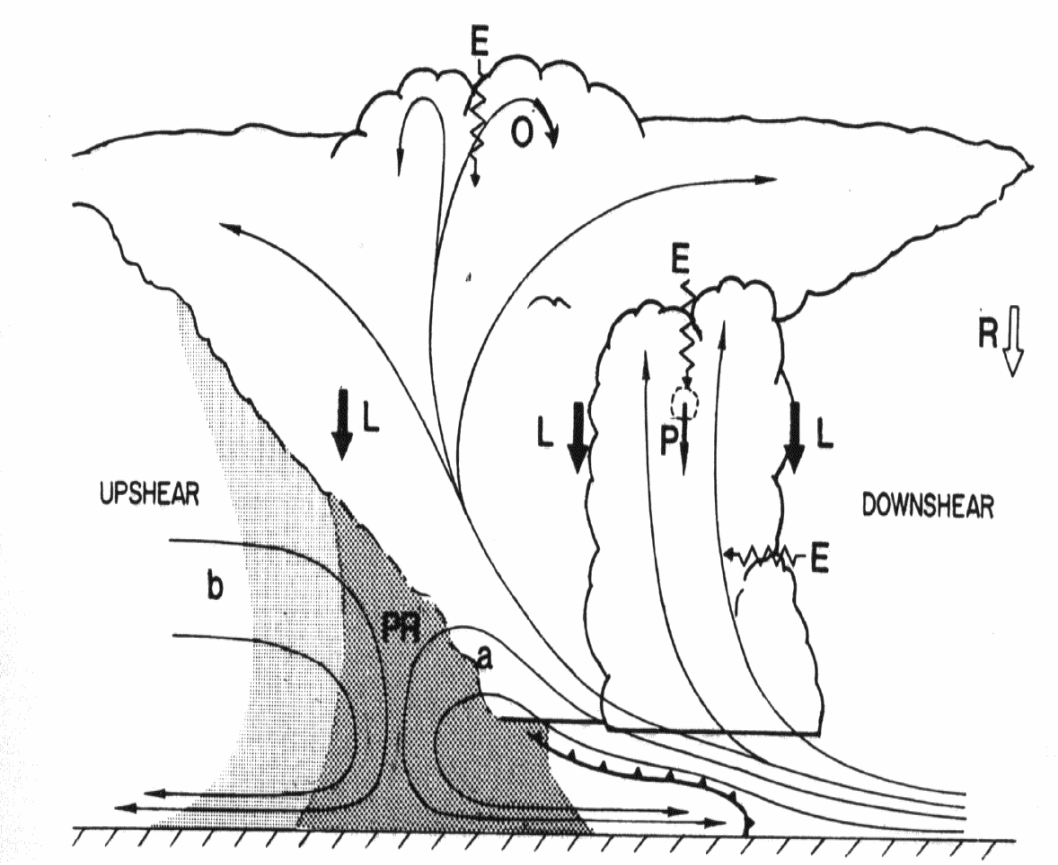


FIGURE 2.3:> Schematic of updraft, downdraft, and entrainment flows within a typical Cb. based on a composit of observational studies, numerical model studies, and research by the authors. All flows are storm relative. From Knupp and Cotton (1985).

Srivastava concluded that stronger downdrafts were associated with steeper environmental lapse rates, higher amounts of rainwater, and higher environmental relative humidity. The third conclusion is counter-intuitive: dry environmental air entrained into the downdraft would seemingly produce stronger vertical velocities by enhancing evaporation, but the author suggested that negative buoyancy is enhanced in moist environments because the water vapor increases the environmental virtual temperature. As a result, the virtual temperature difference between the downdraft and its environment is larger, and the downdraft is stronger.

Observational and three-dimensional cloud model results were used by Knupp (1988) to examine downdrafts within high plains cumulonimbi. The model allowed both melting

and evaporation, and was used to look at low level, precipitation associated downdrafts only. He found that the downdraft was forced by precipitation loading, negative buoyancy from evaporation, sublimation, and melting, and pressure forces. Maximum amplitude of the downward acceleration occurred in the 1-2 km layer, where all three forcing mechanisms had the same sign.

Additional model simulations were performed by Proctor (1988) and Proctor (1989), serving to specifically study microbursts. He used a two-dimensional, time-dependent model to examine the evolution of microburst structure after initiation. In Part I of his study, the downdrafts were initialized by introducing hail near cloud base and allowing the melting and sublimation of the hailstones to drive the negative buoyancy. Part II described a few model runs in which snow is introduced instead of hail. He concluded that the particular type of hydrometeor is important in the overall structure of the resulting microburst. Those initialized with snow tended to be more narrow but produced microbursts of similar magnitudes as those initialized with hail. None of the model runs presented by Proctor initialize a downdraft with liquid rain. He also concluded that microbursts can be either wet or dry (depending on whether liquid precipitation exists as the microburst approaches the surface), and that stronger microbursts are associated with an dry, unstable boundary layer.

More recent investigations of convective downdrafts have attempted to improve upon numerical weather model cumulus parameterizations. The pioneering work of Arakawa and Schubert remains the most complete theory, but other authors have attempted to make improvements, especially with regard to the inclusion of downdrafts. Cheng and Arakawa (1997) used a combined updraft-downdraft model which includes a rainwater budget and

convective downdrafts. The downdraft portion of the model includes only the liquid phase, and the vertical momentum equation includes thermal buoyancy and water loading. Unlike Srivastava and other authors, Cheng and Arakawa use an evaporation scheme which depends on the relative humidity of the column and the amount of available rainwater. Resulting downdrafts can be either saturated or unsaturated. Inclusion of downdrafts indeed eliminates excessive cumulus drying in the lower part of the cloud layer, a deficiency of the updraft-only model.

Technological innovations other than computers and models have also been very important in understanding convective downdrafts. Obtaining observations of downdrafts is crucial to learning whether model results are correct. Aircraft measurements are possible, but can be very dangerous within intense thunderstorms. Therefore, remote sensing technology, like Doppler radar, is extremely useful in understanding convective storm structure.

2.3 Doppler Radar

The science of radar meteorology was born during World War II, in the early 1940 s. Scientists used a 10 cm S-band radar to track rain showers. Theoretical work on Mie Scattering Theory during the late 1940 s improved the science by showing how precipitation-sized particles scatter electromagnetic radiation.

Doppler radar was introduced in the 1950 s and described in a series of Weather Radar Conference papers. Holmes and Smith (1958) tested a simple, low-powered Doppler radar in an attempt to measure speeds of particles within a tornado. They experienced

numerous problems, including attenuation and clutter, but this pioneering work set the stage for the development of more advanced radar technology. Lhermitte (1968) made some of the first attempts to use multiple Doppler radars to obtain three-dimensional particle movement within a convective storm. If assumptions were made about particle terminal velocities, vertical velocities of the air could be estimated by calculating divergence at several grid points. However, computer power severely limited scientists ability to use these methods in a timely manner.

Brandes (1977) used dual-Doppler techniques to study three-dimensional flow in severe thunderstorms. He observed a forward-flank downdraft, and hypothesized about the source of the downdraft air. Rotation within the storm was also analyzed. This was one of the earliest studies using dual-Doppler radar to examine convective downdrafts. Fujita and Wakimoto (1983) studied microbursts using a three Doppler radar network. A third radar eliminates ambiguity when a target lies along the line connecting two radars.

Today, fast processors, a powerful network, and excellent Doppler radar spatial coverage allow meteorologists to view radar images of virtually any storm in the country a few minutes after the data is collected. Radial velocity signatures within thunderstorms are examined to look for rotation, and tornado warnings can be issued several minutes before the storm strikes to give people time to seek shelter. Additionally, universities and research institutes conduct field projects in which two or three Doppler radars are placed in position to sample passing storms. Large datasets, including polarimetric information, are obtained and analyzed so that clouds and thunderstorms can be better understood. Doppler radar will undoubtedly continue to be instrumental for both forecasting and convective storm research.

CHAPTER 3

Convective Downdraft Model

3.1 Introduction

In order to better understand the behavior of convective downdrafts given different atmospheric conditions, a simple one-dimensional model has been developed. The model is based primarily on equations used by Cheng and Arakawa (1997), but with important simplifying assumptions. After establishing a pre-storm environmental sounding, precipitation is introduced into sub-saturated air, where it evaporates and cools the surrounding air, producing a downdraft. Steady-state solutions to water vapor and rainwater budget equations are found, and profiles of vertical velocity, water vapor, and rainwater are obtained. Section 3.2 provides a detailed description of the model, including the governing equations, microphysical parameterizations, entrainment formulation, discretization, and computational methods.

3.2 Model Description

a. Basic Equations

The downdraft model is one-dimensional and steady-state, and consists of budgets of mass, vertical momentum, moist static energy, water vapor, and rainwater. It allows for evaporation of rainwater and entrainment from the updraft and the environment.

Conservation of mass is given by

$$\frac{dm}{dz} = \varepsilon - \delta, \tag{3.1}$$

where m is the downdraft mass flux, ε is the rate of mass entrainment per unit height, and δ is the rate of mass detrainment from the downdraft per unit height.

Conserving moist static energy,

$$\frac{d}{dz}mh = \varepsilon\bar{h} - \delta h, \tag{3.2}$$

where h is the moist static energy of the downdraft and $\bar{h}$ is the moist static energy of the environment. Moist static energy is defined as $h = c_p T + gz + Lq$, where c_p is the specific heat at constant pressure, T is the temperature of the downdraft, g is gravity, z is the height above ground level, L is the latent heat of vaporization, and q is the water vapor mixing ratio of the downdraft.

The water vapor budget equation can be expressed as

$$\frac{d}{dz}mq = \varepsilon\bar{q} - \delta q + E, \tag{3.3}$$

where $\bar{q}$ is the water vapor mixing ratio of the environment and E is the source of water vapor due the evaporation of rainwater. Microphysical parameterizations will be presented in the next section. The vertical momentum equation is expressed as

$$\frac{d}{dz}mw = -\rho\sigma\frac{(B - gq_r)}{1+\gamma} - \delta w, \tag{3.4}$$

where w is the vertical velocity (where positive is defined downward), σ is the cross sectional area of the downdraft, γ is the virtual mass coefficient, taken to be 0.5 following Cheng and Arakawa (1997), and B is the thermal buoyancy, given by

$$B = g\frac{(T_v - \bar{T}_v)}{\bar{T}_v}, \tag{3.5}$$

where T_v is the virtual temperature of the downdraft, and $\bar{T}_v$ is the virtual temperature of the environment. Virtual temperature is defined as

$$T_v = T(1 + 0.608q). \tag{3.6}$$

Equation (3.4) shows that downward momentum can be created both by rainwater loading and by negative thermal buoyancy, which is obtained when the virtual temperature of the downdraft is less than the virtual temperature of the surrounding environment (3.5). No entrainment term appears in (3.4) because the environmental vertical velocity is assumed to be negligible.

The rainwater budget equation is given by

$$\frac{d}{dz}\rho\sigma q_r(w + V_t) = R - E, \tag{3.7}$$

where ρ is the density of the downdraft, q_r is the rainwater mixing ratio, V_t is the terminal velocity of the falling rain, given by

$$V_t = 36.34(\rho q_r)^{0.1364}\left(\frac{\rho}{\rho_0}\right)^{-0.5}, \tag{3.8}$$

which has units ms^{-1}, E is the source of water vapor due to evaporation of rain, and R is the rain flux from the updraft to the downdraft Equation (3.8) shows that raindrop terminal velocity depends only upon the amount of rainwater (and a density correction); raindrop size distribution is not considered.

In equation (3.7), R is the rain flux from the updraft to the downdraft, which is formulated following Cheng (1989). Consider a cylindrical updraft, tilted at an angle θ with the vertical. Rain falls from the tilted updraft into the downdraft, as shown in Figure 3.1. V_t again represents the terminal velocity of the raindrops, except that here it refers to drops falling from the updraft. Then $V_t \sin\theta$ is the component of the velocity of the falling rain in the direction of the arrow. Multiplying this quantity by ρq_r gives the rain flux from the updraft to the downdraft:

$$Flux_{u-d} = \rho q_r V_t \sin\theta . \tag{3.9}$$

The desired quantity, R, needs to have units $kgm^{-1}s^{-1}$, and R is defined as per unit height. Multiplying equation (3.9) by the diameter of the cylinder, $2a$, should therefore give us the rain flux from the updraft to the downdraft:

$$R = (2a\rho q_r V_t \sin\theta)_u , \tag{3.10}$$

where the subscript u refers to updraft quantities. In order to express (3.10) in terms of the cross sectional area of the updraft, multiplying by σ and dividing by $\sigma = \pi a^2$ gives

$$R = \left(\frac{2}{\pi a}\rho\sigma q_r V_t \sin\theta\right)_u \quad kgm^{-1}s^{-1} . \tag{3.11}$$

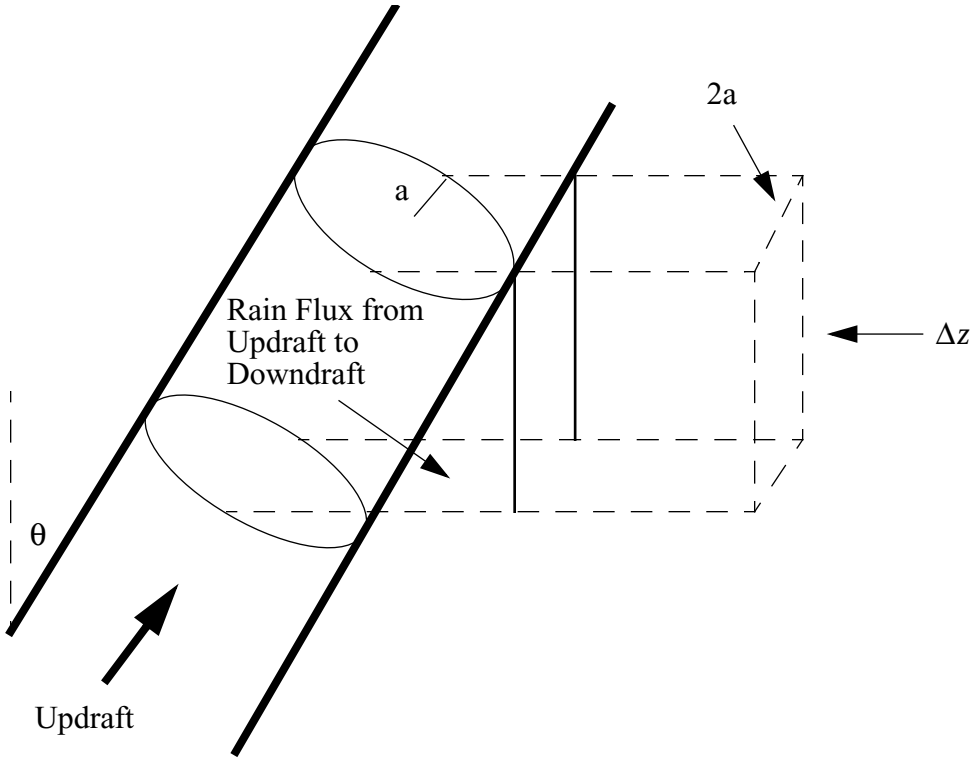


FIGURE 3.1:>Tilted cylindrical updraft with associated downdraft. The updraft cylinder has radius *a*, and a vertical section with height Δz is shown. Rain falls from the tilted updraft into the downdraft, and the rain flux is calculated normal to the updraft side.

b. Microphysical Parameterizations

Following Klemp and Wilhelmson (1978), evaporation is parameterized as follows:

$$E = \sigma\left(1 - \frac{q}{q_s}\right) C \frac{(1000\rho q_r)^{0.525}}{5.4\times10^5 + \dfrac{2.55\times10^6}{(pq_s)}}, \tag{3.12}$$

where q_s is the saturation water vapor mixing ratio of the downdraft, *p* is the atmospheric pressure expressed in *mb*, and *C* is the ventilation coefficient given by

$$C = 1.6 + 124.9(1000\rho q_r)^{0.2046}. \tag{3.13}$$

In both (3.12) and (3.13), the factor of 1000 is used to correct for differences in units in the Klemp and Wilhelmson (1978) paper. MKS units will be used here unless otherwise specified. From (3.12), the amount of evaporation increases as the relative humidity of the downdraft decreases, and as the amount of rainwater increases. However, if $q = q_s$, the downdraft is saturated, and no evaporation occurs.

c. Entrainment

Entrainment is probably the least understand component of convective updrafts and downdrafts. We define entrainment as the process by which air originating either in the environment or the updraft enters the downdraft. The formulation below loosely follows Cheng and Arakawa (1997), but several of the details have been changed. Since the change in the downdraft s cross-sectional area with height is directly related to entrainment, we begin with a derivation of an expression for $\frac{d\sigma}{dz}$.

Two processes that can affect the change of the downdraft s cross-sectional area with height will be considered: the increase in area due to the tilt of the updraft, and the decrease in area due to the horizontal convergence of raindrops, or

$$\frac{d\sigma}{dz} = \left(\frac{d\sigma}{dz}\right)_{tilt} + \left(\frac{d\sigma}{dz}\right)_{conv} \tag{3.14}$$

For the tilt term, again consider a tilted cylindrical updraft (Figure 3.1). The downdraft s cross sectional area will change according to the updraft radius, a, and the tilting angle, θ. Looking at a horizontal cross section of the downdraft from above, rain from the

updraft falls into a rectangular area, having width $2a$, and length Δl. This section s incremental area is therefore

$$\Delta\sigma = 2a(\Delta l). \tag{3.15}$$

Next, consider a vertical cross section of the downdraft, as shown in Figure 3.2.

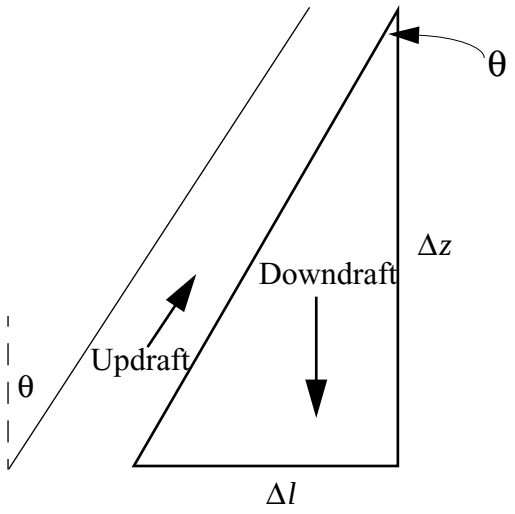


FIGURE 3.2:> Vertical cross section of a downdraft, with tilting angle θ, length Δl, and height Δz.

From this schematic, it can easily be seen that $\tan\theta = \frac{\Delta l}{\Delta z}$, or $\Delta l = \Delta z \tan\theta$. Substituting this into (3.15), $\Delta\sigma = 2a(\tan\theta)(\Delta z)$, or

$$\left(\frac{d\sigma}{dz}\right)_{tilt} = 2a(\tan\theta). \tag{3.16}$$

In order to find $\left(\frac{d\sigma}{dz}\right)_{conv}$, we first differentiate $m = \rho\sigma w$ with respect to z:

$$\frac{dm}{dz} = \rho w\frac{d\sigma}{dz} + \sigma\frac{d}{dz}(\rho w). \tag{3.17}$$

Next, assume temporarily that no entrainment or detrainment occurs; this is equivalent to saying that $\frac{dm}{dz} = 0$ from equation (3.1). Using this assumption in (3.17), and substituting from equation (3.14), we get

$$\left(\frac{d\sigma}{dz}\right)^{*}_{conv} = -\frac{\sigma}{\rho w}\frac{d}{dz}(\rho w) - \left(\frac{d\sigma}{dz}\right)_{tilt}. \tag{3.18}$$

The asterisk is used to denote that a temporary assumption has been made, and this is not the final equation. In Figure 3.3, the upright column represents a downdraft, and the shading represents rain falling within the downdraft. The velocity of the air within the rain-

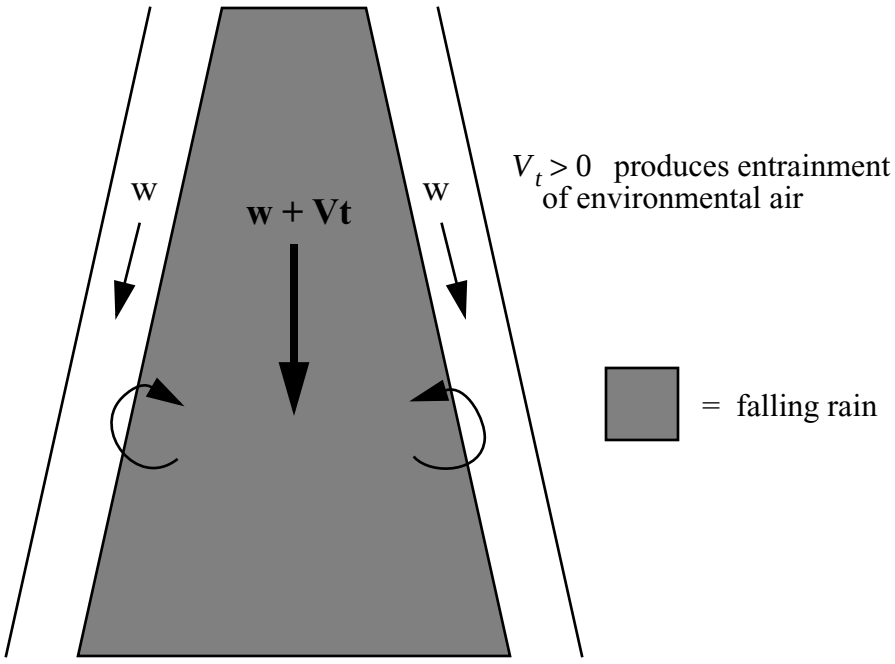


FIGURE 3.3:> Vertical cross section of a precipitating downdraft, where the shaded region represents falling rain. Air within this area falls at a greater velocity than air near the downdraft edge, so horizontal vorticity is produced, leading to entrainment of environmental air.

filled area is $w + V_t$, where V_t is the terminal velocity of the raindrops. However, near the edge of the downdraft, falling rain does not contribute to the total downward velocity,

so the total velocity is simply *w*. This difference is associated with horizontal vorticity near the edge of the downdraft, resulting in environmental air being entrained into the downdraft s edge. If $V_t = 0$, entrainment by this mechanism would not occur. Therefore, the assumption made above that $\frac{dm}{dz} = 0$ is essentially the same as saying that $V_t = 0$. To correct for the error associated with this assumption, Cheng and Arakawa (1997) equate the ratio between $\left(\frac{d\sigma}{dz}\right)_{conv}$ and $\left(\frac{d\sigma}{dz}\right)^{*}_{conv}$ with the ratio between the downward air velocity at the edge of the downdraft and the downward air velocity within the falling rain, or

$$\frac{\left(\frac{d\sigma}{dz}\right)_{conv}}{\left(\frac{d\sigma}{dz}\right)^{*}_{conv}} = \frac{w}{(w + V_t)} < 1 \tag{3.19}$$

Substituting (3.19) into (3.18),

$$\left(\frac{d\sigma}{dz}\right)_{conv} = -\left(\frac{w}{w + V_t}\right)\left[\frac{\sigma}{\rho w}\frac{d}{dz}(\rho w) + \left(\frac{d\sigma}{dz}\right)_{tilt}\right]. \tag{3.20}$$

Therefore,

$$\frac{d\sigma}{dz} = 2a(\tan\theta) - \left(\frac{w}{w + V_t}\right)\left[\frac{\sigma}{\rho w}\frac{d}{dz}(\rho w) + 2a(\tan\theta)\right]. \tag{3.21}$$

To better understand how entrainment is formulated, we substitute (3.14) into (3.17):

$$\frac{1}{m}\frac{dm}{dz} = \frac{1}{\sigma}\left[\left(\frac{d\sigma}{dz}\right)_{tilt} + \left(\frac{d\sigma}{dz}\right)_{conv}\right] + \frac{1}{\rho w}\frac{d}{dz}(\rho w) \tag{3.22}$$

Substituting for $\left(\frac{d\sigma}{dz}\right)_{conv}$ from equation (3.20), and adding, we get

$$\frac{1}{m}\frac{dm}{dz} = \frac{V_t}{w + V_t}\frac{1}{\sigma}\left(\frac{d\sigma}{dz}\right)_{tilt} + \frac{V_t}{w + V_t}\frac{1}{\rho w}\frac{d}{dz}(\rho w) . \tag{3.23}$$

Rearranging,

$$\frac{1}{m}\frac{dm}{dz} = -\frac{V_t}{w}\frac{1}{\sigma}\left(\frac{d\sigma}{dz}\right)_{conv} . \tag{3.24}$$

Examining (3.24) and (3.20), we see that $\frac{1}{m}\frac{dm}{dz}$, which is essentially net fractional entrainment, is zero when $V_t = 0$, and is proportional to $\frac{a}{dz}(\rho w)$ and $\left(\frac{d\sigma}{dz}\right)_{tilt}$. Net entrainment therefore occurs when the downdraft accelerates downward, but detrainment occurs if $\frac{d}{dz}(\rho w)$ becomes sufficiently negative, which can happen when the downdraft becomes positively buoyant and slows down rapidly with height.

An obvious drawback to this formulation is the requirement that V_t must be non-zero for entrainment or detrainment to occur. The problem is greatest when dealing with a positively buoyant downdraft, because in reality, a downdraft striking a stable layer should slow down and spread horizontally outward, regardless of whether falling rain exists within it. Therefore, a correction to the above formulation is presented later, when we discuss a downdraft impinging on a temperature inversion.

d. Discretization

The equations presented in section *a* total a system of 6 first-order, non-linear differential equations. Due to their nonlinearity, an analytic solution is not possible, so they must be discretized. A vertical grid is therefore created (Figure 3.4). The top of the grid repre-

sents the origin of the downdraft; variables at this level will be given the subscript $i = 0$. Level 2, or $i = 1$, is located a distance Δz from the top. Several parameters will need to be defined at half-grid levels; these will be assigned the subscripts $i + \frac{1}{2}$ or $i - \frac{1}{2}$.

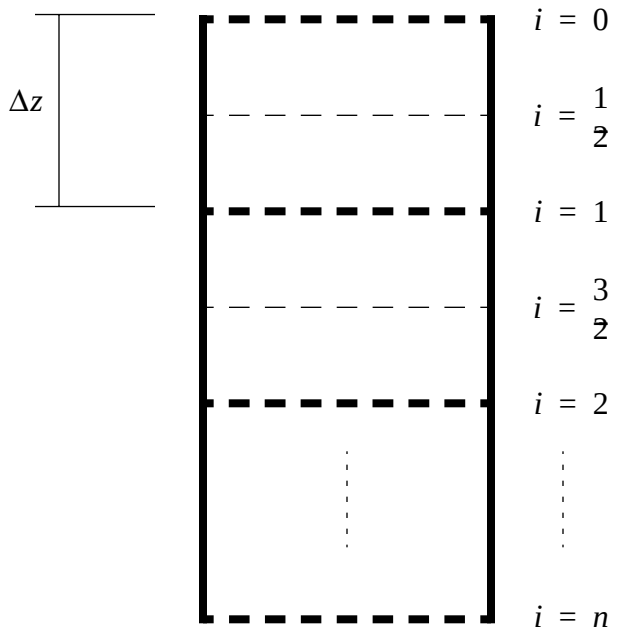


FIGURE 3.4:> Vertical grid on which the downdraft will be placed. Downdrafts will originate at the top of the grid, where $i = 0$, and continue to level n. The distance from level 0 to level 1 is Δz.

Using a centered difference approximation, a discrete version of equation (3.1) can be written as

$$\frac{(m_i - m_{i-1})}{\Delta z} = (\varepsilon - \delta)_{i-\frac{1}{2}}. \tag{3.25}$$

Therefore, entrainment and detrainment, ε and δ, are defined at the half-grid levels, while mass flux is defined at the integer grid levels.

Next, the moist static energy budget, equation (3.2), can be written in a similar fashion. Using a centered difference approximation,

$$\frac{[((mh)_i - (mh)_{i-1})]}{\Delta z} = (\varepsilon\bar{h})_{i-\frac{1}{2}} - (\delta h)_{i-\frac{1}{2}}. \tag{3.26}$$

Multiplying the discrete version of the continuity equation, (3.25), by $h_{i-\frac{1}{2}}$ and subtracting the result from (3.26), the detrainment terms cancel and we are left with

$$\frac{\left[\left(m_i\left(h_i - h_{i-\frac{1}{2}}\right) - m_{i-1}\left(h_{i-1} - h_{i-\frac{1}{2}}\right)\right)\right]}{\Delta z} = \varepsilon_{i-\frac{1}{2}}\left(\bar{h}_{i-\frac{1}{2}} - h_{i-\frac{1}{2}}\right). \tag{3.27}$$

Using an upstream formation, we set $h_{i-\frac{1}{2}} = h_i$. After making the substitution, and solving for h_i, equation (3.27) becomes

$$h_i = \frac{\left[h_{i-1} + \Delta z\left(\frac{\varepsilon}{m}\right)_{i-\frac{1}{2}}\bar{h}_{i-\frac{1}{2}}\right]}{\left(1 + \Delta z\left(\frac{\varepsilon}{m}\right)_{i-\frac{1}{2}}\right)}. \tag{3.28}$$

Examining the above equation, we see that the moist static energy at grid-level *i* is simply an interpolation between the environmental moist static energy at $i - \frac{1}{2}$ and the downdraft moist static energy at level $i - 1$.

Next, we need to formulate the discrete form of the water vapor budget equation. Making another centered difference approximation, equation (3.3) becomes

$$\frac{[((mq)_i - (mq)_{i-1})]}{\Delta z} = (\varepsilon\bar{q})_{i-\frac{1}{2}} - (\delta q)_{i-\frac{1}{2}} + E_{i-\frac{1}{2}} \tag{3.29}$$

As with the moist static energy equation, we multiply equation (3.25) by $q_{i-\frac{1}{2}}$ and subtract the result from (3.29). Once again, the detrainment terms cancel, leaving

$$\frac{\left[\left(m_i\left(q_i - q_{i-\frac{1}{2}}\right) - m_{i-1}\left(q_{i-1} - q_{i-\frac{1}{2}}\right)\right)\right]}{\Delta z} = \varepsilon_{i-\frac{1}{2}}\left(\bar{q}_{i-\frac{1}{2}} - q_{i-\frac{1}{2}}\right) + E_{i-\frac{1}{2}}. \tag{3.30}$$

Making the approximations $q_{i-\frac{1}{2}} = q_i$ and $m_{i-\frac{1}{2}} = m_{i-1}$, substituting equations (3.12) and (3.13), and solving for q_i, we get

$$q_i = \frac{\left[q_{i-1}\left(1 - \frac{\Delta z A}{m_{i-1}}\frac{1}{q_{s_i} + q_{s_{i-1}}}\right) + \Delta z \frac{\varepsilon_{i-\frac{1}{2}}}{m_{i-1}}\bar{q}_{i-\frac{1}{2}} + \Delta z \frac{A}{m_{i-1}}\right]}{\left(1 + \Delta z \frac{\varepsilon}{m_{i-1}} + \frac{\Delta z A}{m_{i-1}}\frac{1}{q_{s_i} + q_{s_{i-1}}}\right)}, \tag{3.31}$$

where

$$A = \frac{\left[\sigma_{i-\frac{1}{2}} C\left(1000\rho_{i-\frac{1}{2}} q_{r_{i-\frac{1}{2}}}\right)^{0.525}\right]}{5.4\times10^5 + \left(\frac{2.55\times10^6}{p_{i-\frac{1}{2}} q_{s_{i-\frac{1}{2}}}}\right)}. \tag{3.32}$$

Equation (3.4), the momentum budget equation, is discretized by first making a centered difference approximation:

$$\frac{[(mw)_i - (mw)_{i-1})]}{\Delta z} = -(\rho\sigma)_{i-\frac{1}{2}} \frac{\left(B_{i-\frac{1}{2}} - g q_{r_{i-\frac{1}{2}}}\right)}{1 + \gamma} - (\delta w)_{i-\frac{1}{2}}. \tag{3.33}$$

Multiplying equation (3.25) by $w_{i-\frac{1}{2}}$ and subtracting the result from (3.33), we get

$$\frac{\left[\left(m_i\left(w_i - w_{i-\frac{1}{2}}\right) - m_{i-1}\left(w_{i-1} - w_{i-\frac{1}{2}}\right)\right)\right]}{\Delta z} = -(\varepsilon w)_{i-\frac{1}{2}} - (\rho\sigma)_{i-\frac{1}{2}} \frac{\left(B_{i-\frac{1}{2}} - g q_{r_{i-\frac{1}{2}}}\right)}{1+\gamma} \tag{3.34}$$

Assuming that $w_{i-\frac{1}{2}} = w_i$ and rearranging, we get

$$w_i = \frac{\left[w_{i-1} - \frac{(\Delta z)}{m_{i-\frac{1}{2}}}\left(\rho_{i-\frac{1}{2}}\sigma_{i-\frac{1}{2}} \frac{\left(B_{i-\frac{1}{2}} - g q_{r_{i-\frac{1}{2}}}\right)}{1+\gamma}\right)\right]}{1 + \frac{\left(\Delta z \varepsilon_{i-\frac{1}{2}}\right)}{m_{i-\frac{1}{2}}}}. \tag{3.35}$$

The thermal buoyancy, defined by equation (3.5), is approximated by

$$B_{i-\frac{1}{2}} = \frac{\left(T_{v_{i-\frac{1}{2}}} - \bar{T}_{v_{i-\frac{1}{2}}}\right)}{\bar{T}_{v_{i-\frac{1}{2}}}}. \tag{3.36}$$

Equation (3.9), the rainwater budget equation, can be approximated by

$$[\rho\sigma q_r(w + V_t)]_i = [\rho\sigma q_r(w + V_t)]_{i-1} + \Delta z[R - E]_{i-\frac{1}{2}}. \tag{3.37}$$

Solving for q_{r_i},

$$q_{r_i} = \frac{\left[\rho_{i-1}\sigma_{i-1} q_{r_{i-1}}(w + V_t)_{i-1} + \Delta z\left(R_{i-\frac{1}{2}} - E_{i-\frac{1}{2}}\right)\right]}{\rho_i \sigma_i (w + V_t)_i}. \tag{3.38}$$

The final equation that must be discretized is (3.21), the equation governing the change of the downdraft s cross-sectional area with height. Combining the two terms containing $\tan\theta$,

$$\frac{d\sigma}{dz} = \frac{V_t}{w + V_t}(2a\tan\theta) - \frac{w}{w + V_t}\left(\frac{\sigma}{\rho}\right)\left(\frac{d\rho}{dz}\right) - \frac{\sigma}{w + V_t}\left(\frac{dw}{dz}\right). \tag{3.39}$$

After making a centered difference approximation, and letting $V_{t_{i-\frac{1}{2}}} = V_{t_{i-1}}$,

$w_{i-\frac{1}{2}} = w_{i-1}$, $\left(\frac{d\rho}{dz}\right)_{i-\frac{1}{2}} = \frac{(\rho_i - \rho_{i-1})}{\Delta z}$, and $\left(\frac{dw}{dz}\right)_{i-\frac{1}{2}} = \frac{(w_{i-1} - w_{i-2})}{\Delta z}$, we get

$$\sigma_i = \frac{\left[\sigma_{i-1}\left(1 - \left(\frac{w_{i-1}}{w_{i-1} + V_{t_{i-1}}}\right)\left(\frac{\rho_i - \rho_{i-1}}{\rho_i + \rho_{i-1}}\right) + \frac{1}{2}\left(\frac{w_{i-1} - w_{i-2}}{w_{i-1} + V_{t_{i-1}}}\right)\right) + \Delta z\left(\frac{V_{t_{i-1}}}{w_{i-1} + V_{t_{i-1}}}\right)(2a)\tan\theta\right]}{1 + \left(\frac{w_{i-1}}{w_{i-1} + V_{t_{i-1}}}\right)\left(\frac{\rho_i - \rho_{i-1}}{\rho_i + \rho_{i-1}}\right) + \frac{1}{2}\left(\frac{w_{i-1} - w_{i-2}}{w_{i-1} + V_{t_{i-1}}}\right)} \tag{3.40}$$

e. Computational Procedure

Since multiple variables must be computed simultaneously at each grid-level, several iterative procedures are necessary to obtain accurate results. Before making those calculations, an atmospheric sounding is used to compute the environmental moist static energy, water vapor mixing ratio, saturation mixing ratio, and density. Since density variations between the downdraft and its environment are negligible except for buoyancy effects, we set $\rho_i = \bar{\rho}_i$.

First, we calculate the rain flux from the updraft to the downdraft at every grid-level using equation (3.11). In order to have a better feel for how much rain is being allowed to fall into the downdraft, the precipitation density, $M = (\rho q_r)_u$, is estimated from radar reflectivity measurements. Following Knupp (1988),

$$M = 0.001\left[\frac{Z_e}{2.4\times10^4}\right]^{0.55} \; kgm^{-3} \tag{3.41}$$

for thunderstorm rain. In this equation, Z_e is the value of the radar-derived reflectivity. The terminal velocity of the raindrops within the updraft is also estimated from radar reflectivity. Following Conway and Zrnic (1993):

$$V_{t_u} = 2.6(Z_e)^{0.107} \; ms^{-1}. \tag{3.42}$$

The top of the grid, or grid-level $i = 1$, is defined as the lowest level where the vertical velocity is zero, but is greater than zero below this level. Each downdraft variable can then be initialized as follows: $w_1 = 0$, $\sigma_1 = 0$, $B_1 = 0$, $h_1 = \bar{h}_1$, and $q_1 = \bar{q}_1$. The downdraft rainwater mixing ratio at level 1 is calculated from equation (3.41).

For each grid level beginning with $i = 2$, the following computational steps are taken:

1) Calculate a first guess for σ using equation (3.40).

2) Make an initial guess that $w = 1.0 \; ms^{-1}$.

3) Calculate the first guess for the vertical mass flux: $m = \sigma\rho w$.

4) If the mass flux exceeds its value at the previous level, $\varepsilon = \frac{dm}{dz}$ and $\delta = 0$. If the vertical divergence of the mass flux is negative, $\delta = -\frac{dm}{dz}$ and $\varepsilon = 0$. This assumption is equivalent to estimating the vertical gradient of mass flux as the net entrainment.

5) Calculate the moist static energy using equation (3.28).

6) Make a first guess for the rainwater mixing ratio using equation (3.38).

7) Make a first guess for the temperature of the downdraft using its temperature at the previous grid level.

8) Calculate the saturation mixing ratio of the downdraft from the first temperature estimate.

9) Calculate the mixing ratio of the downdraft from equations (3.31) and (3.32).

10) Update the temperature calculation by using the definition of moist static energy, or

$$T = \frac{1}{c_p}(h - gz - Lq) . \tag{3.43}$$

11) Repeat steps 8-10 until the mixing ratio, saturation mixing ratio, and temperature of the downdraft each converge.

12) Calculate the thermal buoyancy of the downdraft using equations (3.5) and (3.6).

13) Calculate the vertical velocity of the downdraft using equation (3.35).

14) Update the rainwater mixing ratio calculation with equation (3.38).

15) Update the cross-sectional area calculation with equation (3.40).

16) Update the vertical mass flux calculation as in step 3.

17) Repeat steps 4-16 until the values of all variables converge.

The iterations described above converge regardless of the initial guess for *w.* The number of iterations required for convergence varies depending on the particular atmospheric profile, but 2 or 3 iterations are usually sufficient.

f. Summary

The convective downdraft model developed above is a one-dimensional, steady-state, highly simplified model which will be used to examine downdraft structure and intensity. In Chapter 5, several tests will be conducted using the model, including altering the envi-

ronmental stability and varying the amount of precipitation falling into the downdraft. The entrainment formulation explained above will be re-evaluated after examining the model results. Chapter 4 introduces a few case studies in which radar data will be examined.

CHAPTER 4

Detecting Downdrafts with Radar

4.1 Introduction

Doppler radar can be a very useful tool for studying the structure of thunderstorms. Traditional radar only had the capability of detecting precipitation particles within storms, but with the advent of Doppler technology, horizontal motions of the precipitation particles can be inferred. If multiple Doppler radars are available, additional information, including motions in the vertical direction, can be calculated. Therefore, updrafts and downdrafts can easily be studied.

This chapters presents two cases. The first is a supercell thunderstorm in central Oklahoma, and the second is a tropical squall line in the west Pacific. Dual-Doppler radar data is available for both cases, but the analysis for the second case was prepared by other researchers; it is presented to provide an alternative to single-cell thunderstorm down-

drafts. The former case is located in the Atmospheric Radiation Measurement (ARM) Southern Great Plains (SGP) sector, where a dense collection of instruments is available. A third case from the STEPS program in Eastern Colorado and Western Kansas during the summer of 2000 was considered, but the supercellular nature of the observed storm was quite similar to the Oklahoma supercell. In addition, dual-Doppler analysis revealed a strange updraft-downdraft structure, so the results were considered at least as questionable as the ARM case.

4.2 Oklahoma Supercell

a. Case Description

The storm to be studied occurred on 13 June, 1998, in central Oklahoma. A series of supercells formed in a very unstable environment and tracked generally to the east across the Oklahoma City area. The sounding presented as Figure 4.1 was taken from Norman, Oklahoma, shortly before the storms moved through. Weak inversions near 800 *mb* and 500 *mb* prevented storm formation at the time of the balloon launch, but these quickly eroded as afternoon heating reached a maximum. Convective Available Potential Energy (CAPE) values exceeded 3500 Jkg^{-1}, and strong vertical wind shear, including turning winds at low levels, contributed to the instability.

After the storms passed through the Oklahoma City area, authorities evaluated the damage and determined that several tornado touchdowns occurred, as well as hail and straight-line wind damage. In the northern part of the city, a path of straight-line wind

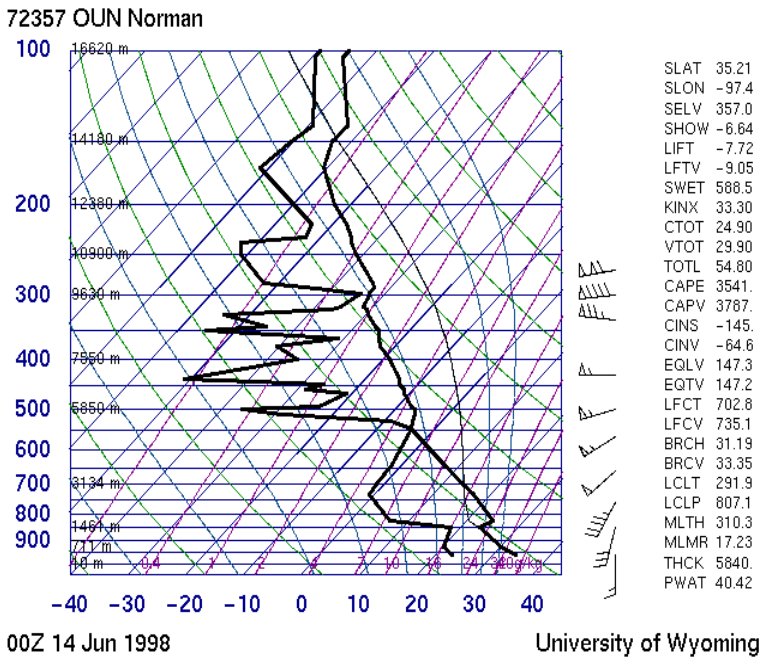


FIGURE 4.1:>The atmospheric sounding from Norman, Oklahoma, at 0Z, 14 June 1998. The dry, unstable layer below 550 mb will be used to simulate the downdrafts.

damage approximately 1.5 miles in width extended 16 miles in length. A media chaser measured a wind gust at 105 *mph* in this area Additionally, a broadcast tower designed to withstand winds of 125 *mph* was toppled (Storm Data, 1998). These straight-line winds occurred in separate locations from the tornado damage, and were likely the result of very strong downdrafts in the core of the thunderstorm.

b. Data and Analysis

Radar data from 13 June 1998 was obtained from the National Severe Storms Laboratory (NSSL) in Norman, Oklahoma. Two Doppler radars lie within 60 *km* of Oklahoma City, and their relatively small distance apart (40 *km*) allows the possibility of dual-Doppler analysis. The Oklahoma City Nexrad radar is located in Norman and has the capability of retrieving reflectivity and radial velocity. NSSL s Cimarron radar is a polarimetric radar which can retrieve reflectivity and radial velocity, as well as several polarimetric

variables. Figure 4.1 is a county map of central Oklahoma showing the location of the two radars. The Nexrad radar, denoted KTLX, is located southeast of downtown Oklahoma City, and the Cimarron radar, Cim, is located to the west. The two circles on the map are the radars dual-Doppler lobes, or regions in which dual-Doppler analysis is a possibility. The beam-crossing angle of the two radars must be larger than a threshold value, so dual-Doppler analysis of a storm lying on a line parallel to the two radars would not be possible. For the particular time of analysis, the supercell studied here lies near the center of the northeastern lobe, in northern Oklahoma County.

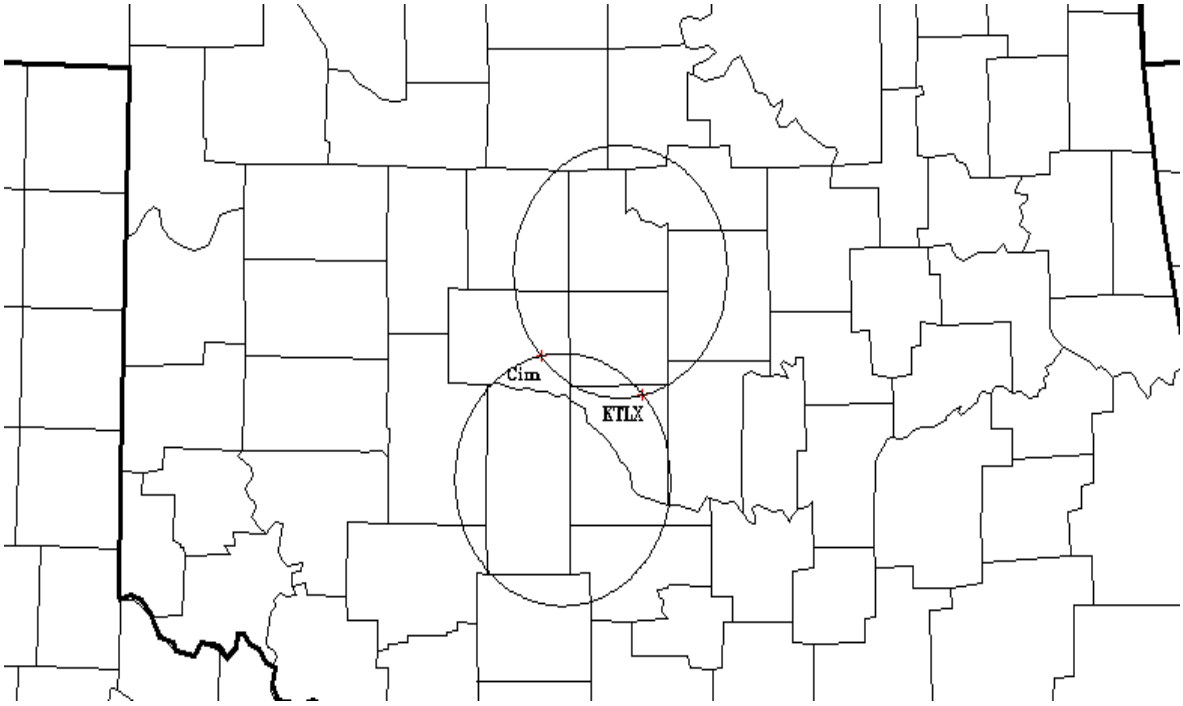


FIGURE 4.2:>A county map of central Oklahoma showing the dual-Doppler lobes. Cim denotes the location of the Cimarron radar, and KTLX denotes the location of the Norman Nexrad radar.

In order to optimize the accuracy of vertical velocity calculations, a full scan of the storm by both radars is necessary. Vertical velocities are derived by calculating the divergence from the two radial velocity measurements at each grid point, then vertically integrating the continuity equation. (This process will be described in more detail later.) If

one or both of the radars do not scan the storm entirely in the vertical, divergence values and therefore vertical velocity values will be missing. It turns out that the Oklahoma City Nexrad (TLX) did not top the storm, so errors and missing values exist. The time of analysis was chosen based on the most complete radar coverage, 0120 Z, or 1920 Central Standard Time. Errors associated with this missing data will be discussed.

The raw radar data is stored in files of each radar scan . A scan consists of sampling the entire storm (or storms) by moving the antenna horizontally between two azimuths, then raising the elevation angle, and repeating. The choices of the elevation angle increments and azimuth limits are made by the radar operator. Each file is given a time, although this time is actually the average time of the entire scan, which usually takes several minutes. Since the data is raw, or unedited, errors associated with the retrieval must be corrected before further analysis is possible. Errors include beam blockage and velocity folding.

Beam blockage results from physical barriers, such as trees, buildings, or mountains, blocking the radar scan. The radar pulse strikes the object and is scattered away, resulting in false reflectivity and radial velocity measurements. This problem usually occurs at low elevation angles because as the antenna is raised, the pulse clears the tree or building in the vertical. Using a software package called Editor, these false measurements can be deleted altogether.

Due to discrete sampling of the phase shift associated with moving precipitation particles, there is a maximum frequency, and therefore maximum radial velocity, which can be retrieved. This value is known as the radar s nyquist velocity. Both CIM and KTLX have nyquist velocities near 30 ms^{-1}, so if velocity measurements exceed this value, the

radar returns values of the same magnitude but of different sign. This problem is known as velocity folding. Fortunately, the Editor package has a feature which allows easy correction for velocity folding. False velocity values are easily identified because of the discontinuity at the nyquist value. Editor then alters the data and obtains the correct radial velocity values. In this case, upper portions of the storm had velocity values greater than 50 ms^{-1} due the very strong jet stream level winds aloft, so a large portion of the high elevation angle velocities had to be unfolded.

After correcting for these errors in the raw data, it is convenient to transfer the data from polar coordinates to cartesian coordinates. A software package from NCAR called Reorder simplifies this process (Oye, 1995). One of the radars is chosen as the base radar: it lies at the origin of the new cartesian plane. The other radar s location is identified by its latitude, longitude, and altitude. Next, the cartesian grid is specified by providing minimum and maximum grid points in all three dimensions, as well as the grid spacing. Reorder then transfers each radar variable into cartesian space.

Since CIM had the most complete coverage, it was chosen as the base radar. To center the storm in the cartesian grid, the *x*-axis extends 105 *km* east of CIM, and the *y*-axis extends 80 *km* to the north. Horizontal grid spacing was chosen to be 1 *km*. In order to capture the highest radar echoes, the vertical axis extends to 20 *km* with grid spacing of 0.5 *km*. Data from KTLX was then placed on the same grid. Some smoothing of the data occurred with this transformation of coordinate systems, but the overall structure of the storm remains unchanged.

The final tool used for radar data analysis is the Custom Editing and Display of Reduced Information in Cartesian space (CEDRIC), developed by NCAR. CEDRIC has

multiple uses, but here it is used only to calculate vertical velocities from the dual-Doppler data. A single radar only retrieves a radial velocity at each grid point; with two radars having different radial velocity measurements from two different angles at each grid point, the horizontal wind components can be calculated (Miller, 1991). Next, the continuity equation,

$$\frac{\partial}{\partial z}(\rho w) + \frac{\partial}{\partial x}(\rho u) + \frac{\partial}{\partial y}(\rho v) = 0\,, \tag{4.1}$$

where u and v are the horizontal wind components, can be integrated vertically to obtain w, the vertical velocity. Equation (4.1) becomes

$$\int_{z_i}^{z_{i+1}} \frac{\partial}{\partial z}(\rho w)\,dz = -\int_{z_i}^{z_{i+1}} \rho\left(\frac{\partial u}{\partial x} + \frac{\partial v}{\partial y}\right)dz\,, \tag{4.2}$$

or in finite difference form (using a centered difference approximation),

$$(\rho w)_{i+1} = (\rho w)_i + \Delta z\left[\rho\left(\frac{\partial u}{\partial x} + \frac{\partial v}{\partial y}\right)\right]_{i+\frac{1}{2}}. \tag{4.3}$$

Therefore, the vertical velocity at the new level is a function of the average divergence between the old level and the new level. CEDRIC allows the option of integrating from the bottom up or the top down. Here, we have chosen to integrate from the top down in order to minimize potential errors. Since density values are much larger near the surface, integrating from the bottom up makes any error in the divergence calculation larger, so the errors add up quickly and become quite large. The top down approach still has errors, but we hope the errors are less.

Additionally, we must specify a top boundary condition. This is done by estimating from the reflectivity measurements the level at which the vertical velocity is zero, but becomes nonzero at the next grid level down. Usually, with supercell thunderstorms, this

occurs near the tropopause and sometimes even higher (in the case of overshooting tops). For the present case, we have chosen this level to be 18 *km,* which is somewhat arbitrary, but changing this value by a few kilometers does not significantly change the results.

c. Results

The top panel of Figure 4.2 is the horizontal reflectivity of the storm at 1 *km* above the surface. Reflectivity values approach 65 *dBZ* within the precipitation core with very heavy rainfall extending outward. The hooked shape of the reflectivity on the southwest side of the storm is indicative of a supercell thunderstorm with a possible tornado; several tornadoes were indeed reported with this storm. The notch (lower reflectivity values) to the east of the hooked feature is likely the location of an intense updraft, and downdrafts can be expected to the northwest of this area within the region of intense precipitation.

The bottom panel of Figure 4.2 is a vertical cross section along the dashed line in the top panel. The left side of the bottom panel corresponds to the northwest side of the dashed line. Low reflectivity values underneath much higher values near 25 *km* along the cross section indicate the region where a broad, intense updraft is probably located, and a strong downdraft is probably located near 12 *km* within the region of moderate precipitation. Warm, moist air is fed into the updraft of the storm from the southeast. As this air rises, it begins to condense and precipitation is formed in the middle troposphere. Some of the precipitation then falls into the area downwind (to the northwest) of the updraft, and intense downdrafts are formed by the melting and evaporation of precipitation.

Figure 4.3 is an idealized model of a supercell thunderstorm developed by Doswell (1985). The top panel shows the outline of reflectivity measurements (low level precipita-

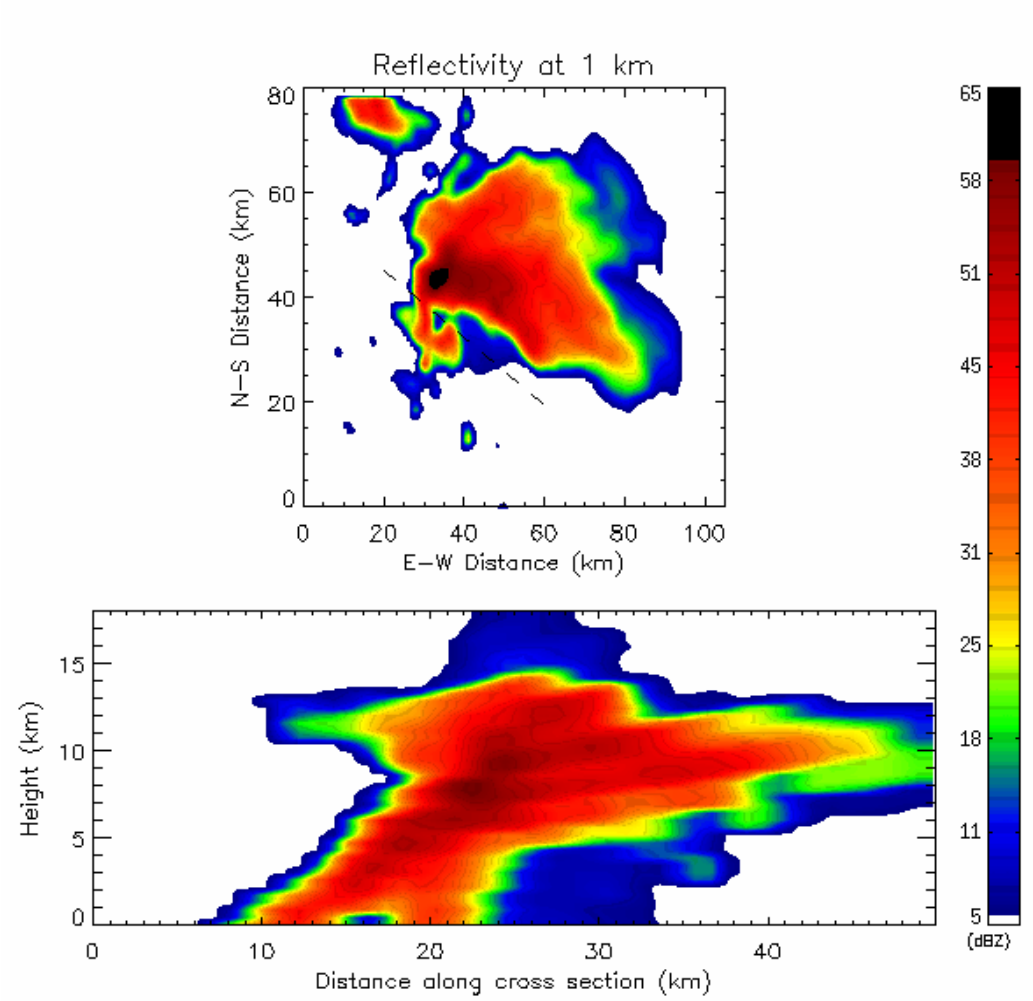


FIGURE 4.3:>Reflectivity measurements of the Oklahoma City supercell. The top panel is a horizontal cross-section at 1 *km* above the surface, and the bottom panel is a vertical cross section along the dashed line in the top panel.

tion) and the bottom panel shows a cross section along the line A-B from the top panel. Note that the direction of the cross-section is reversed from Figure 4.2. The horizontal shape of the model is quite similar to the observed case in Figure 4.2, including the hooked feature and the area of low reflectivity, denoted BWER (Bounded Weak Echo Region). The vertical cross section is similar, but not exactly the same as the model. An area of low precipitation exists, but higher precipitation does not hang over the BWER as shown in the model.

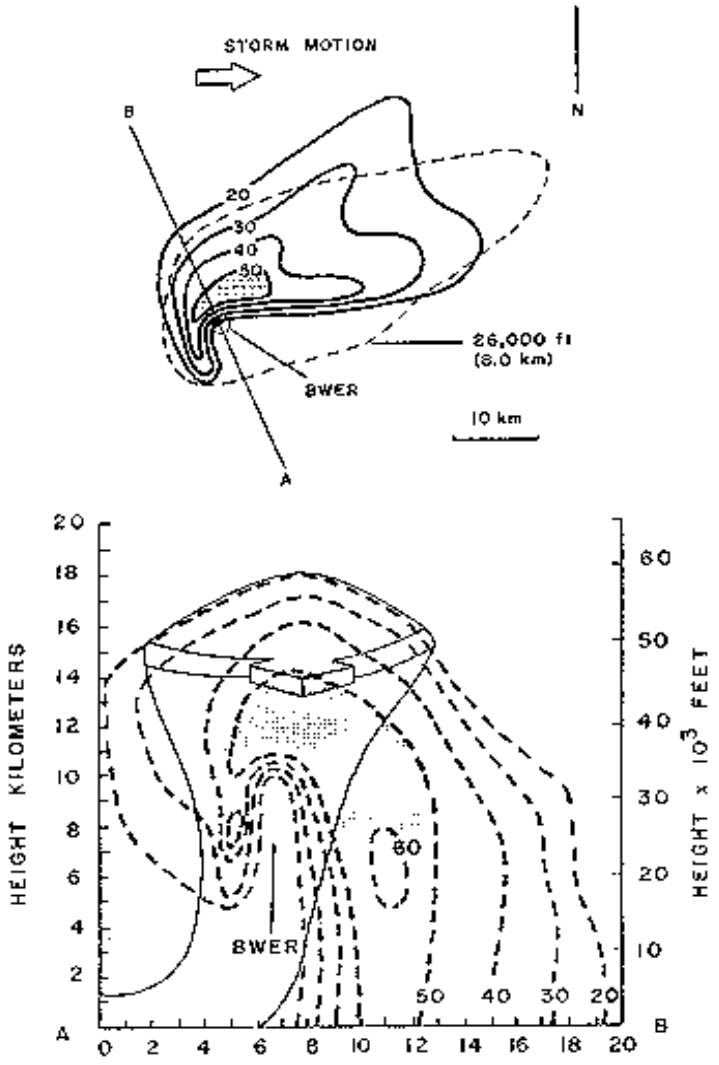


FIGURE 4.4:>Idealized radar cross sections through a supercell thunderstorm. The top panel is the horizontal cross section of reflectivity (*dBZ*), also showing the location of the bounded weak echo region (BWER). The lower panel is a vertical cross section along A-B from the top panel. [From Doswell (1985)]

Figure 4.4 is the dual-Doppler derived vertical velocities of the supercell. The first and most important thing to note is the missing data, especially in the vertical cross-section. As mentioned before, the KTLX radar did not top the storm, so CEDRIC was not able to compute the horizontal wind at some grid points, and therefore vertical velocity values are missing. Since we integrated from the top down, even the values that exist in the low lev-

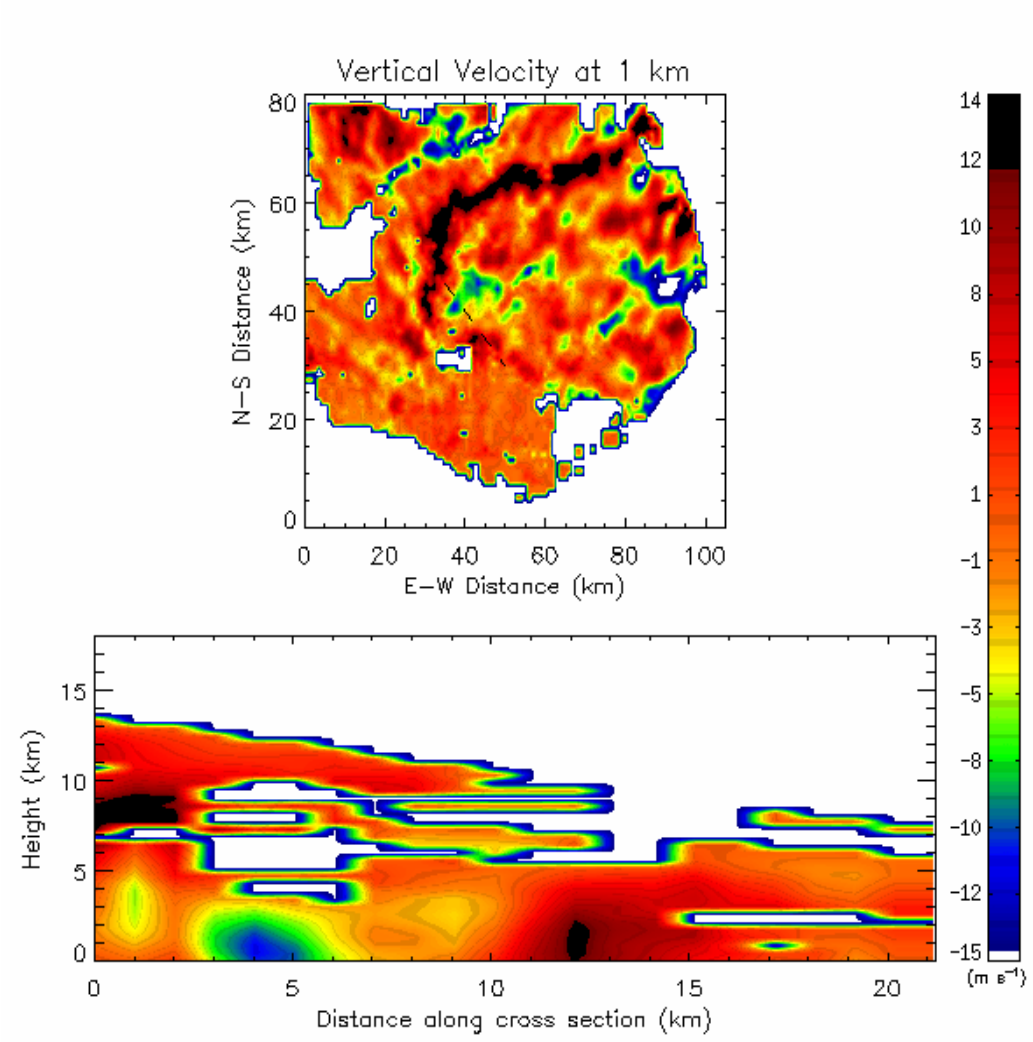


FIGURE 4.5:>Dual-Doppler derived vertical velocity of the Oklahoma City supercell. The top panel is a horizontal cross-section at 1 *km* above the surface, and the bottom panel is a vertical cross-section along the dashed line from the top panel. Note that this cross-section in a slightly different location than in Figure 4.3.

els cannot be fully believed because of the high potential for errors, so the discussion that follows is *assuming* the quantities are accurate.

Note that the location of the cross-section is slightly different than in Figure 4.2. The reason is that there were even more missing values along the original cross-section; this one is shifted slightly to the northeast but still points in the same direction. Positive values represent updrafts and negative values represent downdrafts. Comparing this Figure to 4.2, positive vertical velocities (which now represent updrafts) correspond to the part of

the storm with low reflectivity values, the BWER, as hypothesized. A downdraft approaching 15 ms^{-1} lies along the cross-section, in the middle of the heavy precipitation.

The horizontal cross-section shows updrafts along the northern edge of the storm. This does not fit any supercell thunderstorm model and is probably an erroneous result due to the missing divergence values. Similarly, a strong downdraft is shown on the eastern edge of the storm, and this too, is probably not real. Since these vertical velocity observations are questionably accurate, a second more reliable case is presented.

4.3 Tropical Squall Line

Data for this case was obtained from The Tropical Ocean Global Atmosphere Coupled Ocean-Atmosphere Response Experiment (TOGA COARE), which was carried out from November 1992 to February 1993 over a broad region of the west Pacific. The MIT and TOGA Doppler radars on-board two vessels within this region provided reflectivity and radial velocity measurements of precipitation systems passing through the area. A map of the area with dual-Doppler lobes is provided in Figure 4.5 (taken from the TOGA COARE website).

On 9 February, 1993, a squall line was sampled by the two radars. It moved from the southwest to the northeast and a large portion fell within the dual-Doppler lobes for a few hours. Several papers, including Peterson, Cifelli, et. al. (1999), have documented this case in detail, and members of Dr. Stephen Rutledge s group at Colorado State University provided radar data which has already been synthesized. Reliable vertical velocity calculations were made and are presented here for further analysis.

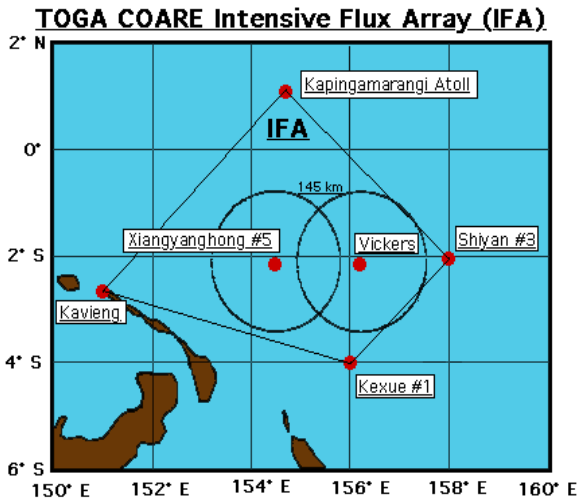


FIGURE 4.6:>Map of the west Pacific TOGA COARE region. The ships carrying the Doppler radars are called Xiangyanghong and Vickers, and the associated dual-Doppler lobes are indicated with overlapping circles.

An environmental sounding was taken shortly before the passage of the squall line and is presented in Figure 4.6. As with the Oklahoma sounding in the previous section, the atmosphere is very unstable throughout most of the troposphere, but an important difference is the amount of moisture. Here, as with most tropical soundings, the entire troposphere is nearly saturated and no dry layers are evident. We therefore expect evaporation of falling rain to be limited since saturation should easily be obtained.

Figure 4.7 gives horizontal reflectivity and a vertical cross-section of the squall line at 1042 UTC. The squall line extends throughout the radars domain but is only about 40 *km* in width. Reflectivity values peak near 40 *dBZ,* so the rain intensity is less than in the supercell case from the previous section. The location of the cross-section is shown with a dashed line in the top panel and is displayed in the bottom panel. Radar echo extend up to about 12 *km*, but the bulk of the heavier precipitation is below 7 *km*. The bull s-eye of precipitation located at 40 *km* along the cross-section is probably a new cell developing along the leading edge of the squall line.

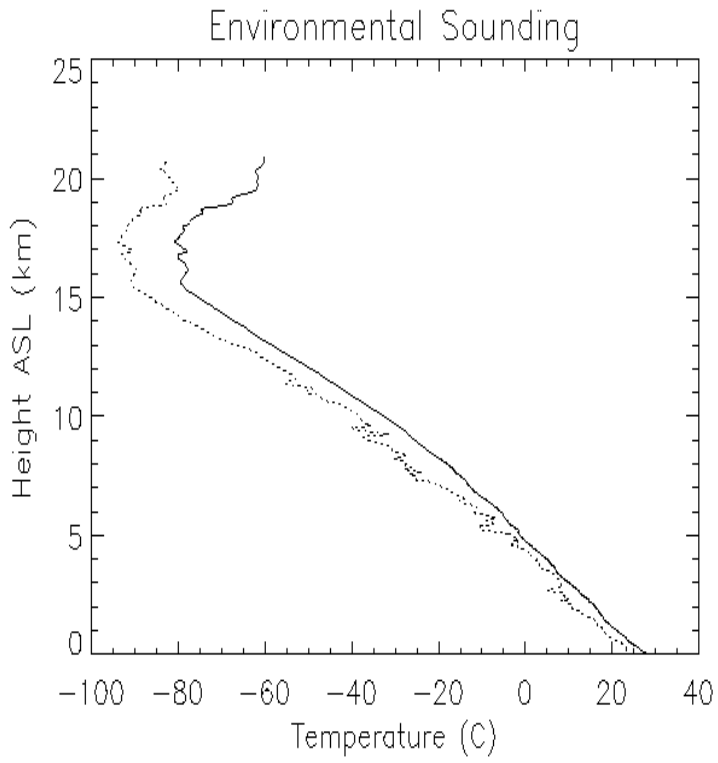


FIGURE 4.7:>Environmental Sounding taken before passage of squall line

Figure 4.8 is exactly the same as 4.7 except vertical velocity is plotted rather than reflectivity. The top panel is a horizontal cross-section at 1 *km ASL* and the bottom panel is a vertical cross-section at the same place as in the previous figure. Positive values (red) represent updrafts and negative values (blue) represent downdrafts. Notice that peak values are only near 5 ms^{-1}, much smaller than in the supercell case. The white notch in the top panel is an area of missing data.

Comparing Figures 4.7 and 4.8, the updraft maximum near 40 *km* along the cross-section corresponds to the location of the new cell. There are no downdrafts evident within this precipitation region so we can conclude that the cell is experiencing its growth stage. Within the center of the heaviest precipitation, about 25 *km* along the cross-section, we

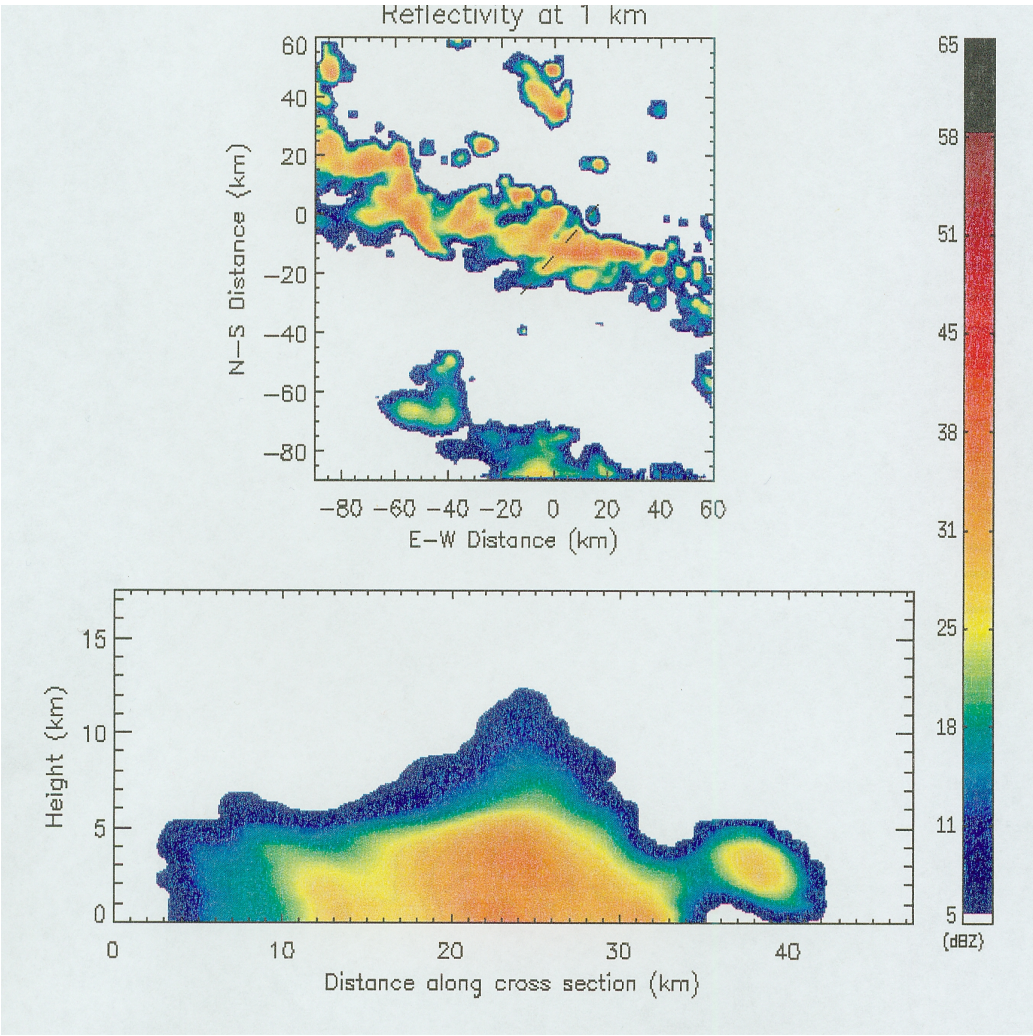


FIGURE 4.8:>Reflectivity of a tropical squall line at 1042 UTC on 9 February 1993 during TOGA COARE. The top panel is a horizontal section at 1 *km* and the bottom panel is a vertical cross-section along the dashed line.

find two downdrafts maxima, peaking between -3 and -4 ms^{-1}. One is located very near the surface, but the other is aloft, between 5 and 6 *km*.

Even though this image is a snapshot in time, we can infer what may be happening as the squall line advances. New cells are forming along the leading edge and are updraft dominant. Precipitation particles are formed and at first evaporate since the environment is subsaturated; this creates the initial downdraft aloft. With time, this downdraft penetrates to the surface and lies within the region of heaviest precipitation. If we took a simi-

lar cross-section a few minutes later, a surface downdraft would probably lie directly below the present location of the downdraft aloft.

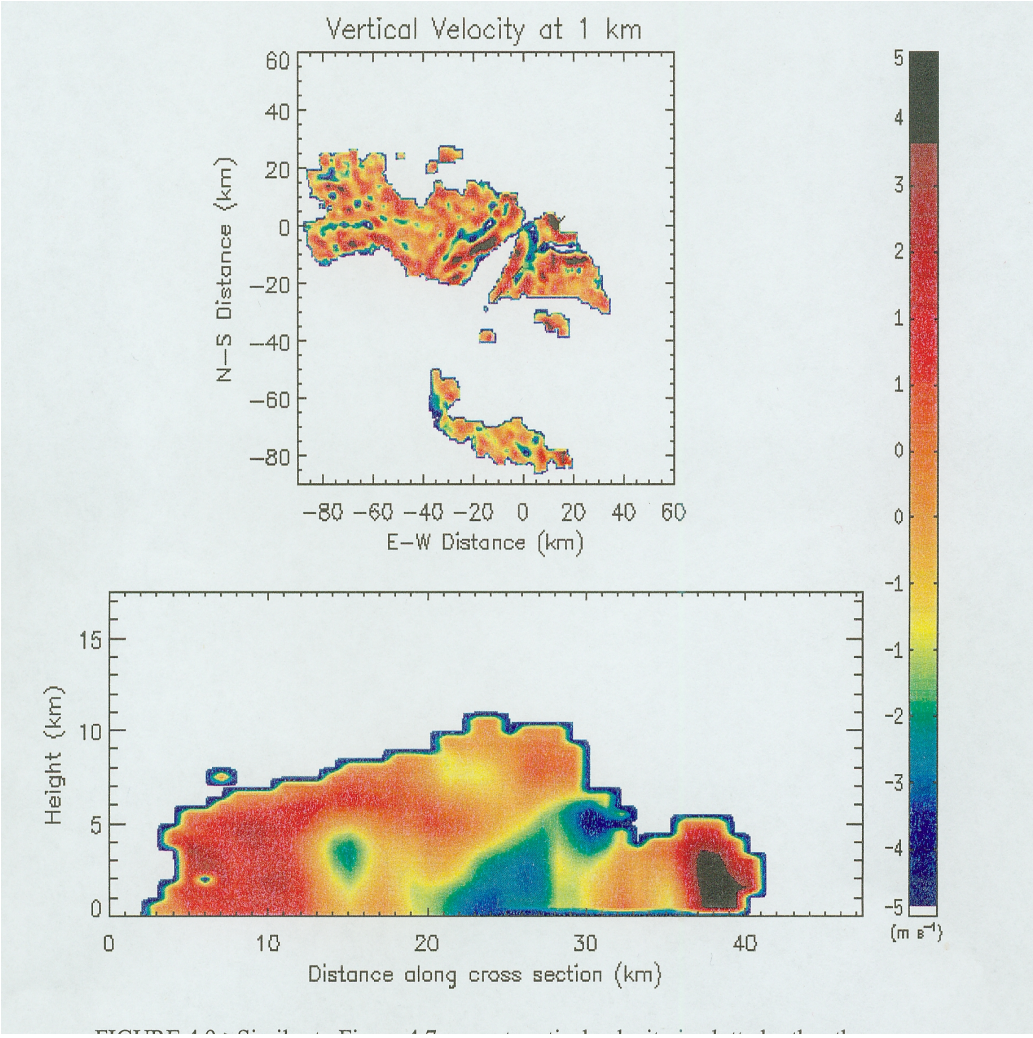


FIGURE 4.9:>Similar to Figure 4.7, except vertical velocity is plotted rather than reflectivity. Positive values represent updrafts and negative values represent downdrafts.

CHAPTER 5

Results and Discussion

5.1 Introduction

This chapter provides the results from the convective downdraft model presented in Chapter 3. Section 2 shows model results from a series of tests in which various parameters, including environmental stability and amount of precipitation, are varied. In section 3, a virga version of the model is discussed, where precipitation falls directly out of a horizontal cloud base into very dry air and downdrafts are produced. Section 4 provides comparisons between model results and the radar data discussed in Chapter 4. Finally, section 5 provides a re-evaluation of the entrainment formulation initially presented in Chapter 3.

5.2 Model Tests

a. Base Case

A series of tests have been developed in which model parameters are varied and the corresponding output are examined. For the first few cases, the same atmospheric sounding is used (Figure 5.1). This is the same sounding as in Figure 4.1, but only the region in which the downdraft will occur is plotted. Notice the dry, nearly dry-adiabatic layer below 5 km. This very unstable layer should be quite conducive for any downdraft to descend to the surface because a negatively buoyant parcel would easily be able to remain cooler than its environment as it descends. The downdrafts will be initiated at 4850 m above sea level, or slightly below the saturated layer in the sounding. Model grid spacing is chosen to be 25 *m*, so there are 154 vertical layers in the grid. Since the environmental sounding does not provide temperature readings every 25 *m*, temperatures and dew points are linearly interpolated between readings.

For the base case, the updraft tilting angle is arbitrarily set to $45°$. Rainfall with a

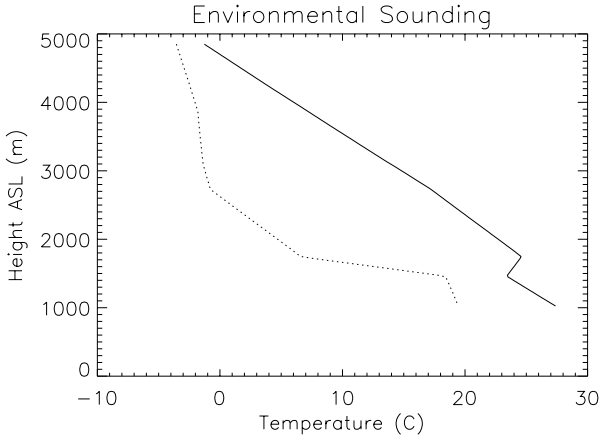


FIGURE 5.1:>The portion of the atmospheric sounding from Figure 4.1 in which the downdraft will be placed. The solid line is the temperature profile and the dotted line is the dew point profile.

radar-equivalent intensity of 50 *dBZ* will fall into the downdraft at all levels and be allowed to evaporate. This rainfall intensity is quite heavy, probably equivalent to a heavy shower during a summer thunderstorm. The cylindrical updraft has radius of 1 *km*. The model stops the downdraft if its vertical velocity changes sign; if it continues to descend, it will be terminated at 1 *km* above the surface since the model is unable to resolve air striking the surface and spreading out. Resulting profiles of vertical velocity, evaporation, thermal buoyancy, rainwater mixing ratio, relative humidity, and cross-sectional area are plotted in Figure 5.2.

The vertical velocity increases at a nearly constant rate in the upper part of the layer, but slows its acceleration as it approaches the surface, reaching a maximum of 13 ms^{-1}. The downdraft s cross-sectional area increases dramatically, and like the vertical velocity, becomes nearly constant near the surface. Even though rainwater continues to fall into the downdraft at all levels, the rainwater mixing ratio drops with decreasing height. This is due to the increasing area of the downdraft, so that the rain source is distributed over a

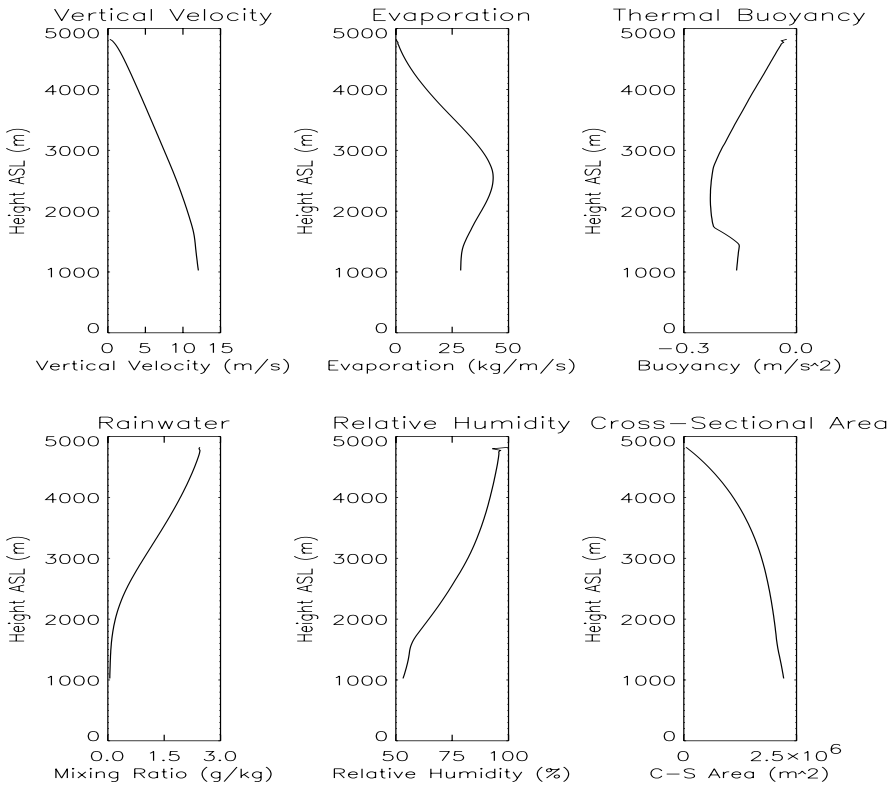


FIGURE 5.2:>Vertical profiles of downdraft vertical velocity, evaporation, thermal buoyancy, rainwater, relative humidity, and cross-sectional area for the base case.

larger area. Evaporation reaches a peak near 2.5 *km* before decreasing when the rainwater supply is greatly diminished. Near the bottom of the downdraft, almost all of the rain falling from the updraft is evaporated.

The downdraft maintains negative thermal buoyancy throughout its descent, but its buoyancy begins increasing just below 2 *km*. Referring back to figure 5.1, this corresponds to an environmental inversion layer. The virtual temperature difference between the downdraft and its environment remains negative, but the magnitude of the difference drops as the downdraft encounters this cooler environmental air. This increase in thermal buoyancy explains why the vertical velocity slows its acceleration near the bottom of the layer.

The downdraft s relative humidity begins with a value equal to its environment, but decreases dramatically as very dry environmental air is entrained into the downdraft (see Figure 3.6 to note the dry environmental layer). As a result, cool, dry air eventually makes it to the surface, probably forming a gust front and cold pool. Model output from the following tests will be compared with this base case.

b. Lower Precipitation Intensity

For this test, precipitation with a radar-equivalent intensity of 30 dBZ falls into the downdraft at all levels; all other parameters remains the same as the base case. The results are plotted in Figure 5.3. Decreasing the amount of precipitation makes an enormous difference: vertical velocity values peak near 3 ms^{-1} before dropping to zero just below 2 *km*. At this point, the downdraft s positive buoyancy eventually causes it to stop descending. Values of evaporation are fifty times smaller than in the base case, so the evaporatively driven negative buoyancy is very small and the downdraft becomes positively buoyant between 2 and 3 *km*. This occurs despite a very unstable environment.

The rainwater goes to zero just below 4 *km*, even though precipitation is still being introduced from the updraft. This occurs because rainwater is defined at the integer grid levels, while evaporation and incoming rain are defined at the half integer grid levels. What is plotted is actually the amount of rain that does not evaporate and falls into the next lower grid level. The downdraft relative humidity drops even more than in the base case because the water vapor source from evaporation is much smaller.

As in the base case, the cross-sectional area increases rapidly and continues to increase, even when the downdraft decelerators. Its value in the lower portion of the layer

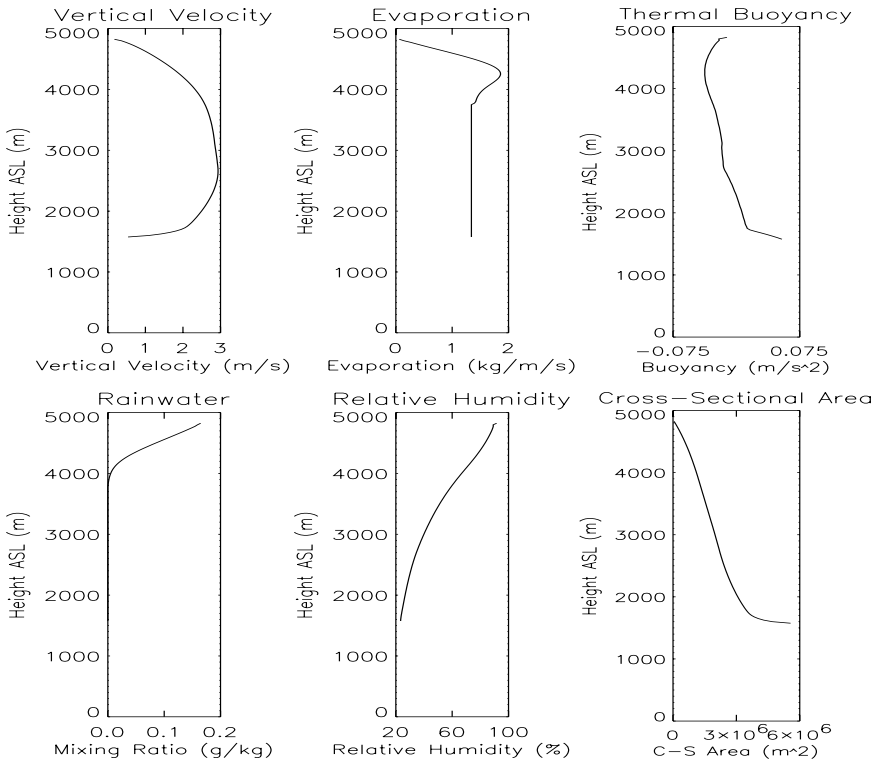


FIGURE 5.3:>Similar to Figure 5.2, except the precipitation intensity is only 30 *dBZ*.

is more than twice as large as the base case. Recall from chapter three that net entrainment is a function of $\frac{\partial}{\partial z}(\rho w)$, so if the downdraft becomes positively buoyant and the vertical velocity begins to rapidly decrease, net detrainment occurs since the mass flux begins decreasing downward. As a result, the downdraft begins to quickly spread outward as it slows down, and the corresponding cross-sectional area increases dramatically just before the downdraft stops.

c. Precipitation Aloft

For the third case, the intensity of the rainfall is changed back to 50 *dBZ*, but precipitation is only introduced above 4 *km* -- below this, no know rainwater is introduced. Figure 5.4 shows that even though less total rainwater falls into the downdraft, its vertical veloc-

ity reaches nearly 12 ms^{-1} , only slightly lower than the base case. The thermal buoyancy profile is nearly identical to the base case, which implies that the vertical velocity difference must be due to less rainwater loading. However, the *small* difference shows that thermal buoyancy plays a much more important role than rainwater loading in driving the downdraft s vertical velocity.

Evaporation and rainwater both go to zero about 1 *km* below where the incoming rain

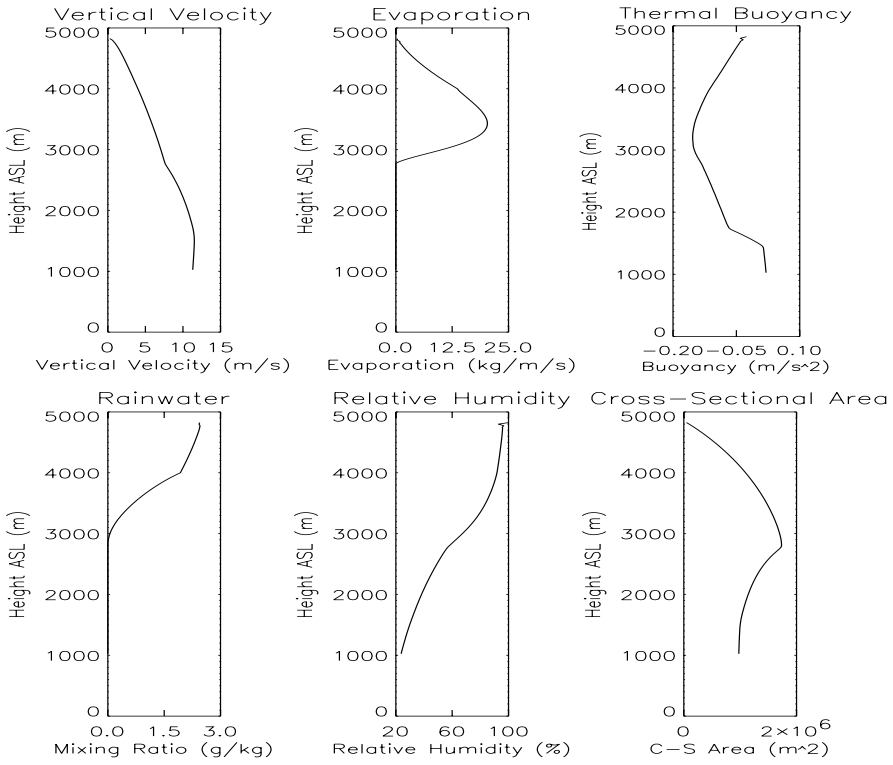


FIGURE 5.4:>Results from 50 dBZ rainfall above 4 *km*

flux ceases. As a result, there are no more raindrops to drive entrainment, and the mass flux levels off and is constant with decreasing height. With constant mass flux and increasing vertical velocity, the cross-sectional area is forced to decrease because $m = \rho\sigma w$ by definition. This result is questionably realistic and is a direct result of the

entrainment formulation explained in Chapter 3. More thorough discussion of this problem will be offered in a later section.

d. High Environmental Relative Humidity

This test serves to examine how the downdraft intensity changes as environmental relative humidity increases. For the base case, the sounding contains a very dry environmental layer throughout the column in which the downdraft descends (Figure 5.1). To test for a relative humidity increase, the temperature profile will be kept the same, but the dew point will be increased at all levels. Figure 5.5 gives the resulting sounding. This is an unrealistic profile since very moist layers rarely have such steep temperature lapse rates, but it is used only to compare with the base case. The results are given in Figure 5.6.

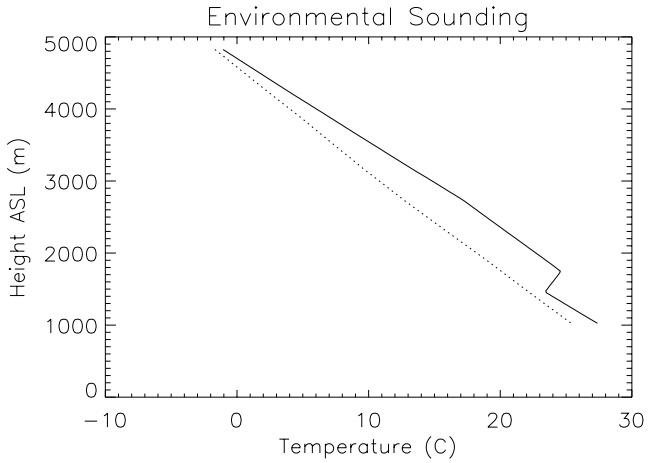


FIGURE 5.5:>Environmental profile in which downdraft will be placed for test d.
The solid line is temperature and the dashed line is dew point.

Vertical velocities are only slightly less than in the base case, peaking near 11 ms^{-1}. Thermal buoyancy values are correspondingly less negative. Interestingly, though, evaporation values are actually as high as in the base case. This seemingly implies that the ther-

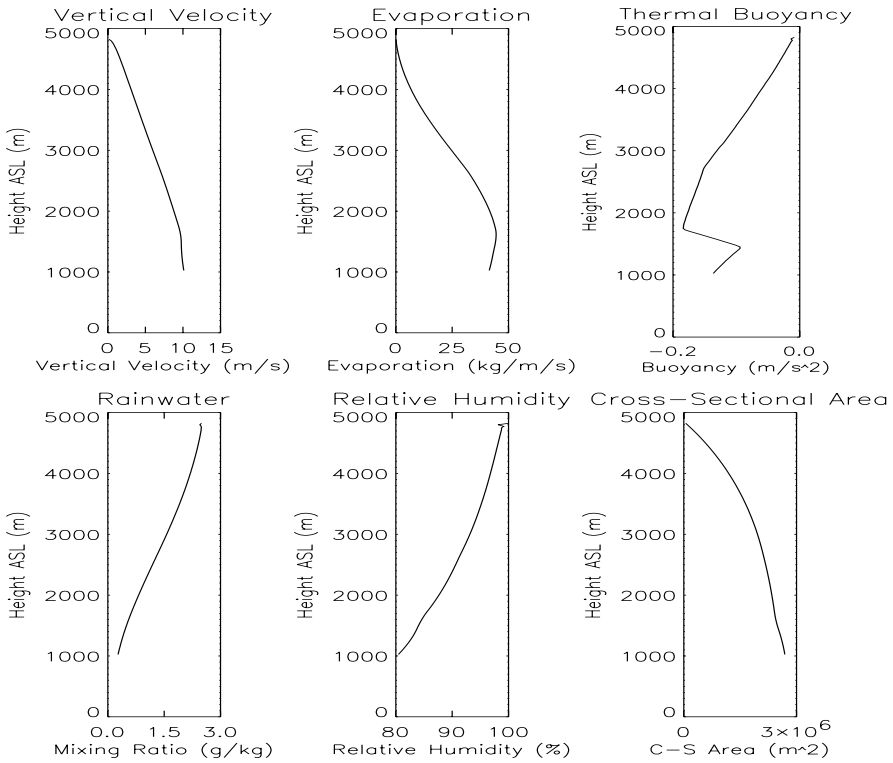


FIGURE 5.6:>Results from increasing environmental relative humidity.

mal buoyancy becoming less negative is not due to less evaporation. One may think that high relative humidity air entrained into a downdraft would limit the amount of evaporation by increasing the downdraft relative humidity. Indeed, relative humidity values in this case are much higher than in the base case, dropping to only 80%. But the largest amount of evaporation occurs higher up in the layer in the base case, diminishing the rainwater supply. In this test, evaporation peaks at a lower level, so the rainwater is not diminished as quickly. The peak in evaporation occurs at the same point as the environmental temperature inversion, so thermal buoyancy values never drop below -0.2 ms^{-2}.

Increasing environmental relative humidity results in higher downdraft relative humidity as mentioned above. It also changes the virtual temperature of both the downdraft and the environment, since virtual temperature is a function of both temperature and water

vapor. This means that adding water vapor to the downdraft without changing its temperature will cause it to be virtually warmer, and therefore more positively buoyant. Likewise, adding water vapor to the environment will cause the downdraft to be more negatively buoyant by increasing the virtual temperature difference. Therefore, changing relative humidity values has complex effects; it alters more than the amount of evaporation. Based on the definition of virtual temperature (equation 3.6), a large water vapor difference between a downdraft and its environment can have a significant effect on the virtual temperature difference, especially if the temperatures are similar. Srivastava (1985) found that increasing environmental relative humidity actually resulted in stronger downdrafts because the environmental virtual temperature is higher. In our test, however, less upper level evaporation and an increase of the downdraft s relative humidity produced a slightly weaker downdraft.

This test shows that increasing environmental relative humidity indeed reduces the downdraft s vertical velocity, but only slightly. An important difference between this and the base case is the nature of the air which reaches the surface. In both cases, the air is cool, but here, it is much more moist. This could be very important with regard to the initiation of future convection.

Another important result concerns the downdraft s actual relative humidity value. Igau, LeMone, and Wei (1999) found that a downdraft s relative humidity is important in determining whether it is positively or negatively buoyant. This is due to the effect of water vapor increasing downdraft virtual temperature. They used data collected with an aircraft during TOGA COARE which penetrated clouds and obtained cloud temperature and vertical velocity measurements, then compared downdraft core values with values

in the surrounding cloud. To calculate virtual temperatures, they had to make guesses about the downdraft relative humidity. They found that the average virtual temperature deviation from the environment for downdraft cores was 0.4 *K*, meaning the cores were *positively* buoyant. However, this result assumes the downdrafts are saturated, with relative humidities of 100%. The authors concede that most downdrafts are subsaturated, but even if relative humidities are much lower, some of the downdraft cores are still positively buoyant.

From Figure 5.5, even with a very moist environmental sounding, the downdraft relative humidity still drops to 80%. This has several implications. First, the downdraft is subsaturated, a result which contradicts other authors assumptions that downdrafts remain saturated. In fact, every test done so far with the model shows relative humidity decreasing as the downdraft descends. An important point is that we have used environmental soundings rather than soundings which may be found within clouds. Downdrafts within clouds are surrounded by saturated air, so entrainment would increase relative humidity values. However, even using a purely saturated environmental sounding, the downdraft still becomes subsaturated.

The second point is better explained referring back to Figure 5.4. This downdraft becomes positively buoyant near the bottom of its descent, but its vertical velocity remains above 10 ms^{-1}. Within this layer, the downdraft is therefore positively buoyant even though it continues to descend. These types of downdrafts are probably what Igau, LeMone, and Wei (1999) observed. They are similar to overshooting tops of thunderstorms, except upside-down. If a very intense downdraft strikes an inversion, it will continue to descend into the inversion layer despite being positively buoyant due to its inertia. Even-

tually, the positive buoyancy will cause the downdraft to stop, unless it reaches the surface first.

5.3 Virga Model

The Virga Model is nothing more than the convective downdraft model presented in Chapter 3 with parameters chosen to simulate evaporating rain falling from a horizontal cloud base. This corresponds to a tilting angle of $90°$ with the vertical. In order to make the model run correctly, equations (3.21) and (3.40) must be altered since $\tan(90°)$ is undefined. This is done by essentially setting the tilting term in the cross-sectional area equation to zero, so that only the convergence term affects the change of the downdraft s cross-sectional area with height. As long as the downdraft remains negatively buoyant and accelerates with decreasing height, it will get smaller. This is a direct result of the entrainment formulation and is probably not realistic. After all rain evaporates, net entrainment goes to zero and the mass flux remains constant. A possible correction for this is presented later in this chapter.

Virga is quite common during the summer in the high plains when the boundary layer is very dry and well mixed. Clouds form above this relatively deep boundary layer and begin precipitating. The rain evaporates as it falls into the dry layer below and the resulting downdraft can easily penetrate to the surface due to the steep environmental lapse rate. These types of downdrafts can be particularly hazardous to aircraft and are often referred to as microbursts.

An atmospheric sounding from Denver, Colorado, is used from 27 August 2001, an afternoon when downdrafts from virga produced very gusty surface winds in Eastern Colorado. The lower portion of the sounding is given in Figure 5.7. The temperature lapse rate is dry-adiabatic and the entire layer is extremely dry. Rain equivalent to 30 *dBZ* is introduced from a cloud base with a diameter of 500 *m*. The observed lifted condensation level (LCL) on this particular day is approximately 5 *km* ASL, so the downdraft will be initiated there. Results are given in Figure 5.8.

The falling rain completely evaporates within the first 1000 *m* of its descent. A down-

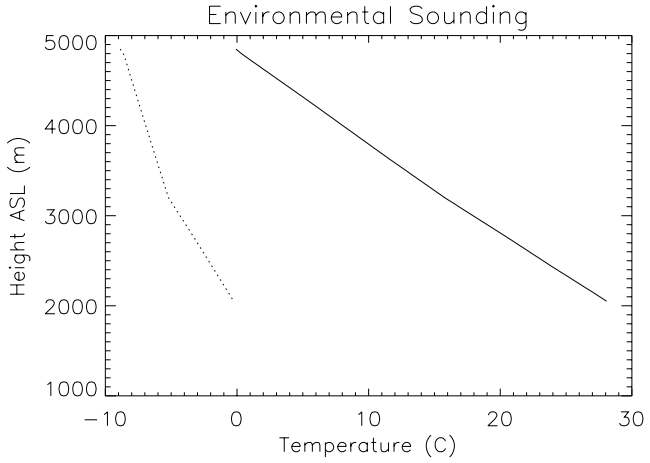


FIGURE 5.7:>Lower portion of an atmospheric sounding from Denver, Colorado, on 27 August 2001 at 0Z

draft is produced and continues to accelerate downward even though evaporation is not occurring. Thermal buoyancy remains negative and is fairly constant, but becomes more negative toward the bottom of the layer. This is probably because the downdraft is drying faster than the environment, making it virtually cooler and therefore more negatively buoyant. As predicted, the cross-sectional area decreases dramatically with height because the mass flux remains constant.

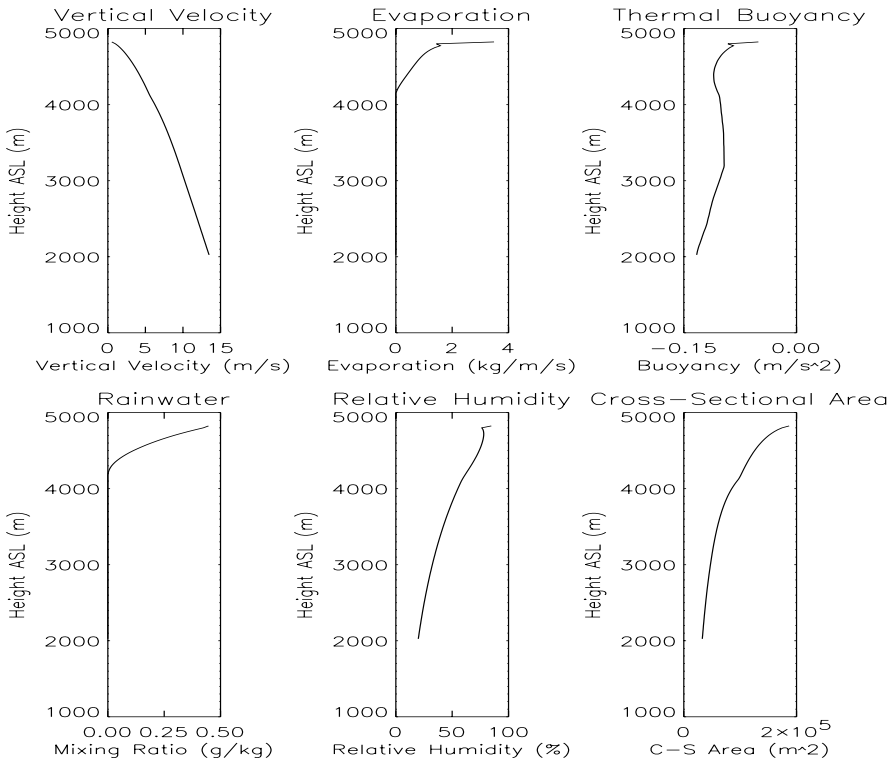


FIGURE 5.8:>Results from the virga version of the model

Further insight into the possible errors in this simulation are provided in Section 5.5. The vertical velocity results seem reasonable, especially considering surface winds were observed between 30 and 40 *mph* on this day in Eastern Colorado. Other factors could influence the strength of the winds, including downward momentum transport and surface friction, so the model is not necessarily a good tool for predicting surface wind speed when virga produces downdrafts.

5.4 Comparison of Radar Data with Model Results

a. Supercell

The purpose of creating the convective downdraft model was not to predict downdrafts in a forecasting sense, but rather to gain insight into the factors contributing to their structure and intensity. The model is far too simplified to expect an accurate depiction of downdrafts within observed thunderstorms because of many factors which are ignored (these will be discussed in Chapter 6). However, since radar data is available in which vertical velocities have been obtained, we will compare the observed data with model output, keeping in mind that we don t expect perfect results.

Using the sounding given in Figure 5.1 (same as the base case) from Norman, Oklahoma, we attempt to use the radar data from the supercell case in Chapter 4 (Figures 4.3 and 4.5) to obtain other inputs into the model. It is impossible to identify an updraft tilting angle from the radar data because sometimes the updraft does not appear to be tilted in a particular snap-shot in time. Thunderstorms are constantly changing, and an updraft can become a downdraft over time if enough precipitation is formed. Updrafts can have both upward and horizontal wind components, so in this respect, it is tilted. For these reasons, we choose $30°$ somewhat arbitrarily. The radius of the updraft is estimated as 2 *km*, although this number is only important in determining the actual values of the downdraft s cross-sectional area. Part of the updraft has no precipitation associated with it, but we are only interested in the portion which contains precipitation. Again, it is very difficult to obtain exact numbers, but based on the maximum reflectivity values observed with radar data, we choose 50 *dBZ* precipitation at the top of the layer, decreasing to 40 *dBZ* near the bottom. This is not within the heaviest precipitation core of the storm, but it is closer to the location of the radar-derived downdrafts. Results are given in Figure 5.9.

As expected, the results are similar to the base case since the same sounding and simi-

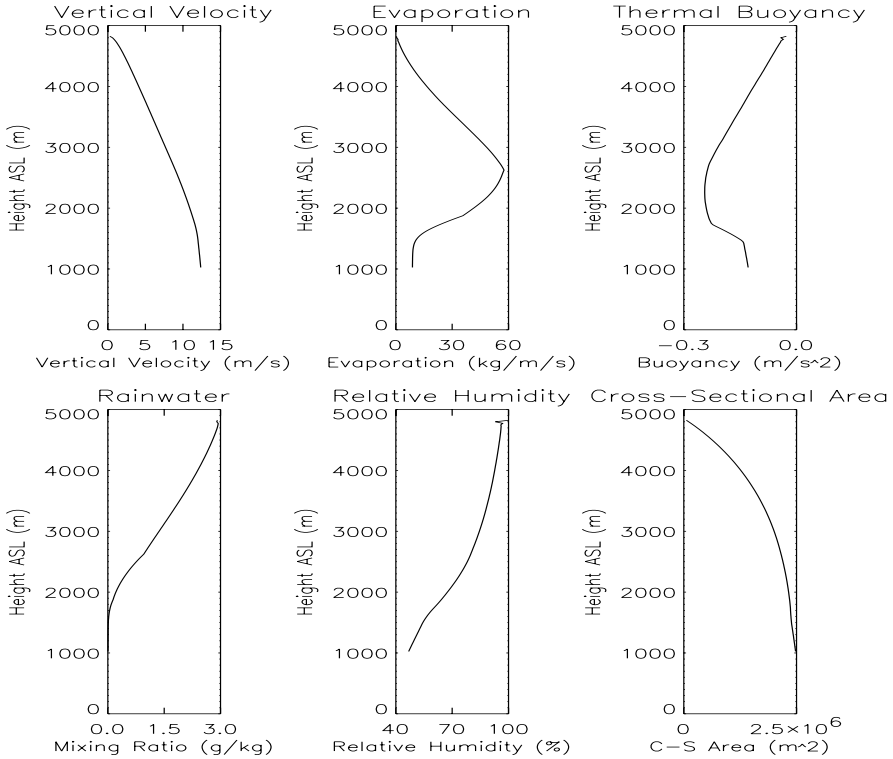


FIGURE 5.9:>Model results using the Norman, OK, sounding and input values based on radar data.

lar precipitation amounts are used. The vertical velocity increases to about 13 ms^{-1} and peaks at the bottom of the layer. From Figure 4.4, the observed maximum downdraft values within the vertical cross-section are near 15 ms^{-1}. These numbers agree fairly well, but it is important to remember that the confidence level in the vertical velocity values obtained using dual-Doppler analysis is quite low. For this reason, we will look at the second, more reliable case.

b. Tropical Squall Line

For this case, the downdraft is initiated at 4750 *km* ASL, or close to the melting level. Figure 5.10 shows the portion of the tropical sounding given in Figure 4.7 in which the

downdraft will be placed. The layer is quite moist and very unstable, with a thin, relatively dry layer about 2.5 *km* ASL. Using the radar data given in Figures 4.8 and 4.9, we again choose an updraft tilting angle of $30°$, updraft radius of 1.5 *km,* and introduce precipitation equivalent to 40 *dBZ* at all levels. According to the radar data, this is the approximate precipitation intensity within the heaviest portion of the squall line, and also the location where we may expect to find a downdraft. Results are given in Figure 5.11.

The simulated downdraft becomes positively buoyant and stops before reaching the

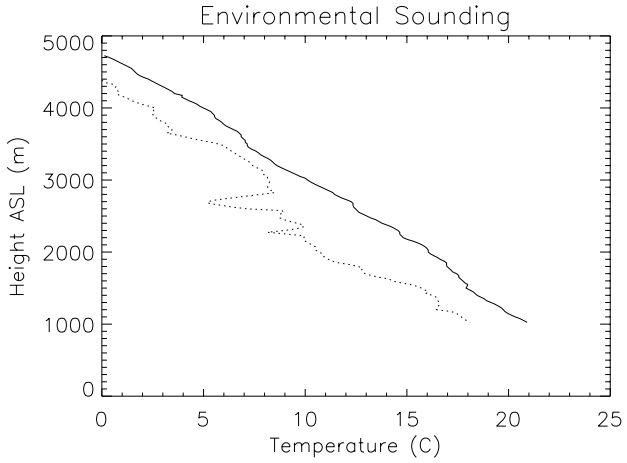


FIGURE 5.10:>Portion of the tropical sounding in which the downdraft will be initiated.

bottom of the model domain. Vertical velocities peak near 3.5 ms^{-1} in the middle of the layer before decreasing rapidly toward the bottom. Even though rainwater is introduced at all levels, the increase in cross-sectional area allows most to be evaporated. When the rainwater supply becomes very low, evaporation decreases and the downdraft becomes virtually warmer than its environment about 2 *km* ASL.

The radar-obtained downward vertical velocities reach almost 5 ms^{-1} within this heaviest precipitation region, but most of the values are between 2 and 4 ms^{-1}. These

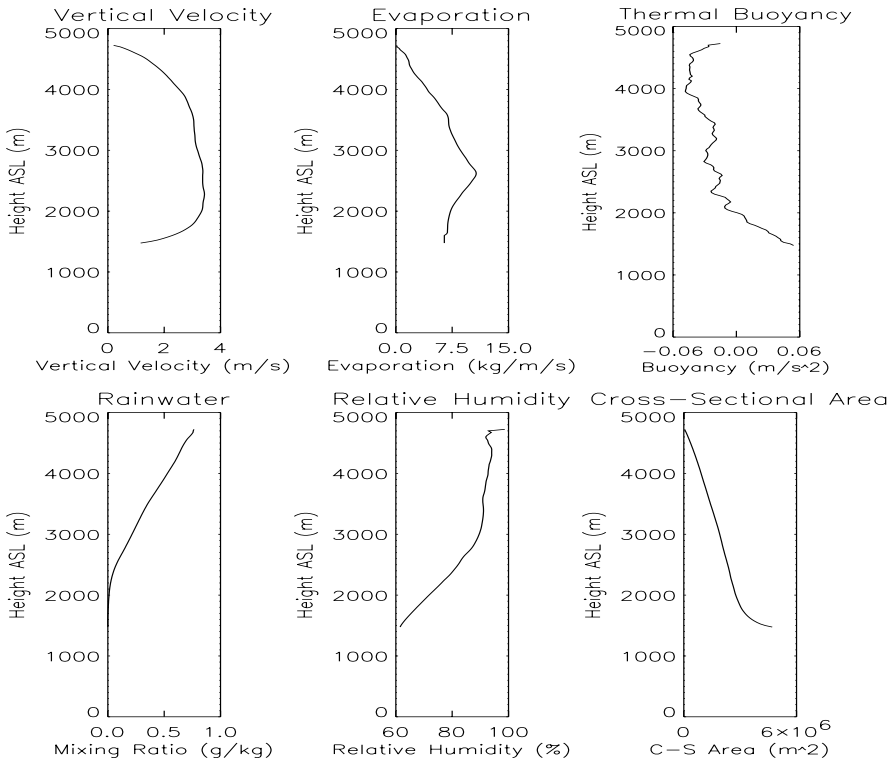


FIGURE 5.11:>Results using the tropical sounding and input parameters derived from radar data

numbers again agree quite well with the model results. It is difficult to make any concrete conclusions based on these findings, however. Given an environmental atmospheric profile and a certain amount of precipitation, the model seems to be able to reasonably predict the intensity of downdrafts which are produced. Since mass flux is also a variable produced by the model, we could also calculate the temperature, humidity, and amount of air pumped into the boundary layer by thunderstorm downdrafts. This is perhaps a more useful and interesting task for a highly simplified model.

5.5 Entrainment Re-Evaluation

This section examines more closely the effects of the entrainment formulation explained in Chapter 3. Recall that net entrainment occurs only when $V_t > 0$, or when rainwater exists within the downdraft column (see Figure 3.3). If all rain evaporates, the downdraft s mass flux must remain constant and no entrainment or detrainment occurs. This is probably not realistic.

An example can be seen by using the virga version of the model presented earlier in this chapter. Figure 5.12 shows the same results as in Figure 5.8, except mass flux and entrainment have been added. Notice that as soon as all the rain evaporates near 4 *km*, the mass flux stops increasing and becomes constant. By definition, the entrainment then goes to zero. Since the downdraft remains negatively buoyant, its vertical velocity continues to increase. Mass flux is given by $m = \rho\sigma w$, so the cross-sectional area is forced to decrease as the vertical velocity increases. This result seems strange. We basically have an inverted dry plume which gets smaller as it descends because it is not allowed to entrain environmental air.

The solution to this problem is unknown because it is virtually impossible to measure entrainment rates. Here, we present another idea which seems more reasonable, but is still probably not correct. The problem with the formulation is greatest when entrainment is not allowed to occur, so the following fix is only applied after all rain evaporates. At that point, the cross-sectional area is fixed and the entrainment necessary to offset the increase in vertical velocity is assumed to occur. Results are shown in Figure 5.13.

The most striking difference from Figure 5.12 is the lower vertical velocity. Since entrainment is now non-zero below 4 *km*, environmental momentum enters the downdraft which serves to slow its descent by making the thermal buoyancy less negative. The mass

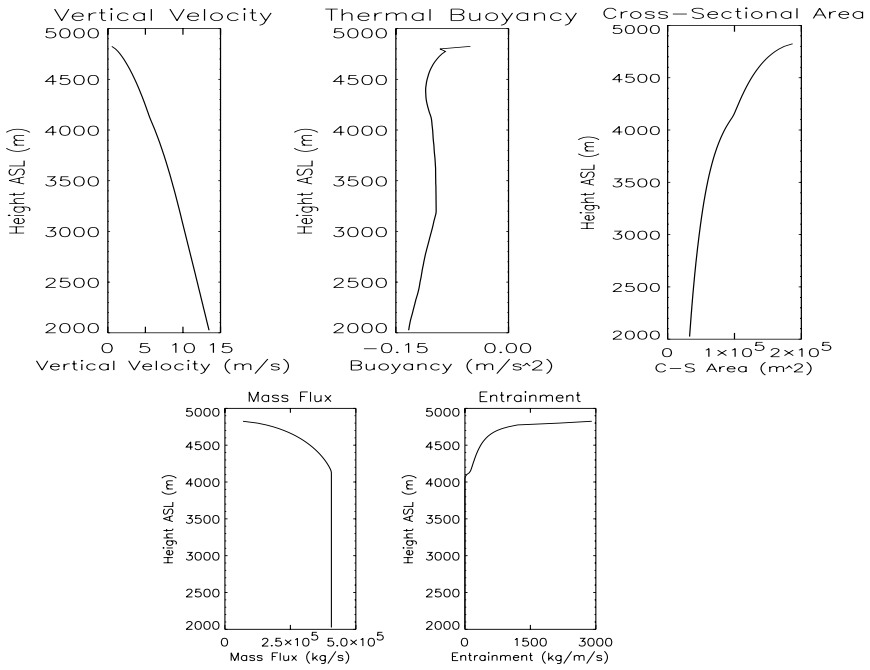


FIGURE 5.12:>Additional results from the virga version of the model.

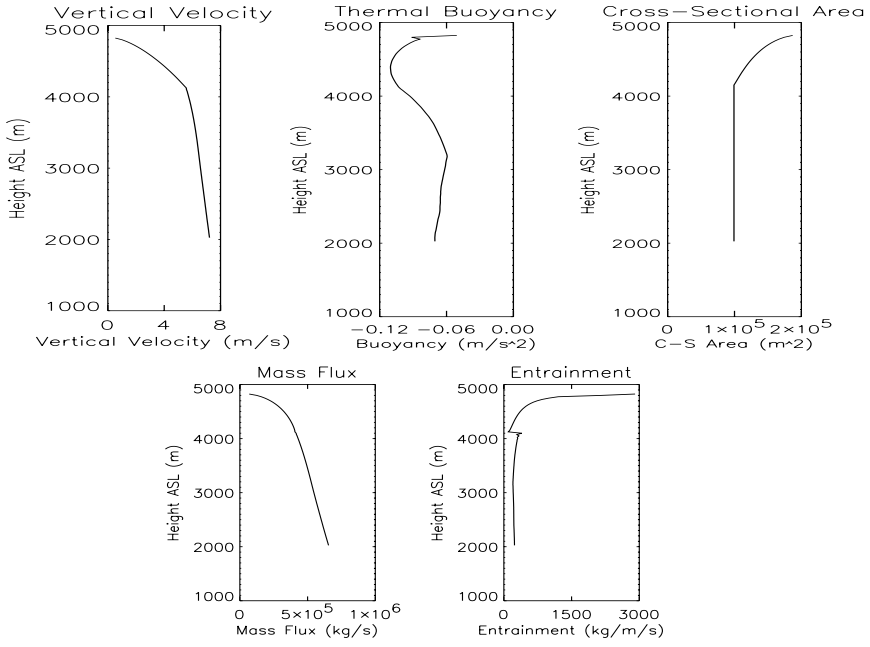


FIGURE 5.13:>Results after fixing cross-sectional area when the rain completely evaporates.

flux continues to increase and the cross-sectional area remains fixed. These vertical velocity values seem too small given such an unstable environmental profile, so perhaps this fix actually allows too much entrainment. A more accurate formulation may therefore

be a compromise between the two. Cross-sectional area would decrease some, but not as much as in Figure 5.12, and vertical velocity values would peak near 10 ms^{-1}.

Another version of this problem could occur when a downdraft becomes positively buoyant, but still does not entrain environmental air or detrain downdraft air. Figure 5.14 gives the same sounding as in Figure 5.7, except a strong temperature inversion has been added near 3 *km* to illustrate this point. Results using this profile are given in Figure 5.15.

The vertical velocity increases until it reaches the inversion, then begins to rapidly

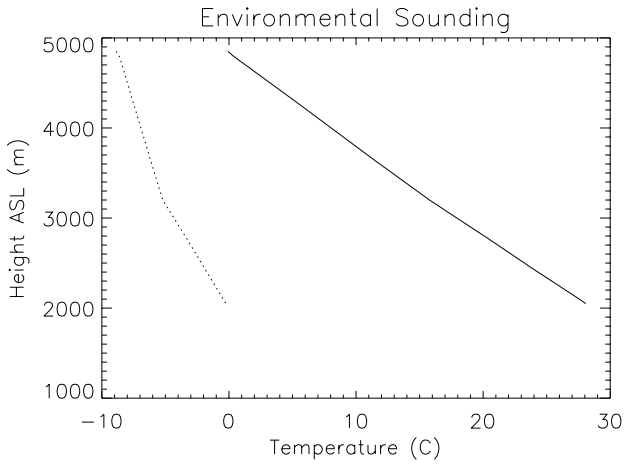


FIGURE 5.14:>Environmental profile used with the vriga version of the model, except with a strong inversion inserted near 3 *km*.

decrease as the downdraft becomes positively buoyant. Mass flux and entrainment values are identical to those in Figure 5.12 since no rain exists within the descending air. The cross-sectional area levels off and begins to increase as soon as the vertical velocity begins to decrease. Although these results seem reasonable, it seems unlikely that a slowing downdraft would not detrain air to its environment.

An important point to note is that the definitions of entrainment and detrainment depend on the definition of a downdraft. If downdraft is simply defined as downward moving air, then an increase is cross-sectional area would not necessarily imply that

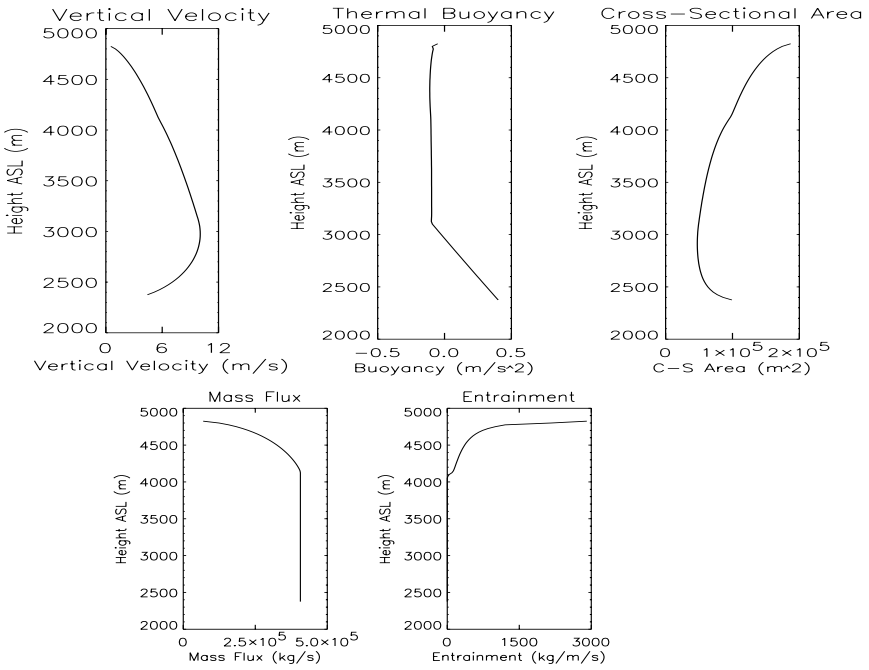


FIGURE 5.15:>Results using the virga version of the model with an environmental sounding given by Figure 5.14.

detrainment has occurred. The downdraft spreads out as it slows but the air contained within remains distinct from the environmental air. Detrainment would imply that downdraft air enters the surrounding air and mixes with its momentum, water vapor, etc. If the downdraft comes to a complete stop, then its air must instantaneously become environmental air.

Whether or not detrainment should really occur is impossible to determine using only this model. We would need more obervations or a more detailed model. It seems reasonable that detrainment should be related to positive buoyancy, so that if a downdraft slows down, it will detrain to its environment. These types of questions are very interesting need to be answered before updrafts and downdrafts can be modeled with a high amount of confidence.

CHAPTER 6

Conclusions

This thesis has used a simple model and Doppler radar data to examine and analyze convective downdrafts. A one-dimensional, steady-state model was developed based primarily on equations used by Cheng and Arakawa (1997). It includes budgets of momentum, moist static energy, water vapor, and rainwater, and outputs vertical profiles of these variables given varying atmospheric conditions. Rainwater falling from a tilted updraft evaporates, cools the surrounding air, and descends as long as it remains negatively buoyant. The strenghts of the downdrafts produced vary greatly depending on the amount of rainwater introduced and the atmospheric profile of the surrounding air.

Doppler radar data was used to examine downdrafts within thunderstorms. These radars are able to detect the radial velocities of precipitation particles, and if two or more radars are used, vertical velocities can also be calculated. Two cases, both with data from two radars, were studied. The first case was a supercell thunderstorm in Oklahoma and fairly intense downdrafts were evident. Missing data from one of the radars prevented a

high confidence level in the accuracy of the vertical velocity values. The second case was a squall line which occurred in the tropical Western Pacific. Less intense downdrafts were observed but complete radar coverage allowed a higher confidence level in the results.

The convective downdraft model was used to perform a series of tests by changing the environmental profile and the amount of rainwater introduced. We are able to draw a series of conclusions based on these tests, but these results could be dependent on several model assumptions and simplifications. Some conclusions include:

-- Downdrafts originating over an unstable environment can reach vertical velocities of at least 15 ms^{-1}.

-- The relative humidity of downdrafts is less than 100%, and if dry environmental air is entrained into the downdraft, its value can drop to less than 20%.

-- Downdrafts can penetrate to the surface even if all of the rain contained within evaporates.

-- Lowering the precipitation amount introduced to a downdraft significantly limits its vertical velocity magnitude because of lower evaporation amounts.

-- Thermal buoyancy plays a much larger role than water loading in driving a downdraft, but water loading can be important in a neutrally stable environment by helping to initiate a downdraft

-- Downdrafts tend to be stronger in relatively dry environments because entrained dry environmental air enhances evaporation; however, moist environments generally have more stable temperature profiles so the buoyancy difference is also related to the difference between the virtual temperatures of the downdraft and its environment.

Many simplifying assumptions were made in developing the model. The first and most important is the steady-state assumption. Thunderstorms are constantly changing, and therefore so are its components: updrafts, downdrafts, etc. A downdraft which entrains environmental air and detrains air to its environment is constantly altering the nature of the surrounding air. This model assumes the surrounding air is the air sampled in a pre-storm sounding. Therefore, the results are probably most accurate shortly after the storm forms, before it has a chance to alter the environment. Additionally, cloudy air has very different properties than non-cloudy air, and this model makes no attempt to describe the nature of air within cumulus or cumulonimbus clouds.

Another assumption is that all water is in liquid form. The downdrafts were initiated below the melting level, but ice particles can certainly exist below this level, especially in strong supercell-like thunderstorms (hail, graupel, etc.) Melting and sublimation would alter the energy profile and certainly affect the results. Additionally, downdrafts can exist well above the melting level, so allowing an ice phase would allow a more thorough investigation into convective downdrafts.

This model is one-dimensional, which limits its ability to accurately model a three-dimensional storm. Atmospheric parameters vary greatly in the horizontal, so to capture these changes, an increase to two or three dimensions would be necessary. Even though the purpose of the model is not to simulate a thunderstorm, adding dimensions would increase the breadth of downdraft testing possibilities.

A final assumption which has been discussed in detail is entrainment. The current formulation only allows entrainment and detrainment if the downdraft contains raindrops.

As a result, a dry plume descending in an unstable environment shrinks in size by several factors. This is not realistic so a better parameterization is needed.

Many of these assumptions and simplifications were made simply because we do not know the exact physics governing certain processes. Traditionally, scientists have used observations and real data to learn about these processes, but this can be a difficult task, especially within intense thunderstorms. Radar is able to remotely sense the large-scale structure of storms, but small-scale processes, such as diffusion, turbulence, and entrainment, cannot be measured. Aircraft data can be useful, but again, flying a plane into a very intense updraft or downdraft containing large hail is very dangerous. Until we find a way to obtain reliable data, many of these questions will remain unanswered.

Testing this simple model with real data is therefore quite difficult. As with any model, it is very important that tests are performed so that the model s reliability can be evaluated. We have attempted to use radar data to test the model s performance, but missing data and coarse resolution prevent confidence in the results. Another possibility is to test the model with a time-dependent, three-dimensional model which includes complex microphysical parameterizations. This could be a useful venture, but often, even these sophisticated models contain questionable parameterizations for processes such as entrainment. They are therefore of no use if the ultimate goal is to understand how entrainment works.

Results presented in this thesis have set the stage for future work. Examples include:

-- Add a time-dependence to the model and study the evolution of downdrafts over time.

-- Make a combined updraft-downdraft model so that the updraft properties do not need to be prescribed.

-- Develop a more reasonable parameterization for entrainment and detrainment, especially in the case when the downdraft contains no raindrops.

-- Find observational data which can be used to test the model s performance.

These examples, along with countless others, need to be addressed before we have before we have a hope for fully understanding convective downdrafts.

REFERENCES

Arakawa, A., and W. H. Schubert, 1974: Interaction of a Cumulus Cloud Ensemble with the Large-Scale Environment. Part I. *J. Atmos. Sci.,* **31**, 674-701.

Betts, A .K., 1976: The Thermodynamic Transformation of the Tropical Subcloud Layer by Precipitation and Downdrafts. *J. Atmos. Sci.,* **33**, 1008-1020.

Brandes, E. A., 1977: Flow in Severe Thunderstorms Observed by Dual-Doppler Radar. *Mon. Wea. Rev.,* **105**, 113-120.

Brandes, E. A., and C. L. Ziegler, 1993: Mesoscale Downdraft Influences on Vertical Vorticity in a Mature Mesoscale Convective System. *Mon. Wea. Rev.,* **121**, 1337-1353.

Byers, H. R., and R. R. Braham, 1949: The Thunderstorm. U.S. Weather Bureau, Washington, D.C., 287 pp.

Carey, L. D., and S. A. Rutledge, 2000: The Relationship between Precipitation and Lightning in Tropical Island Convection: A C-Band Polarimetric Radar Study. *Mon. Wea. Rev,* **128**, 2687-2710,

Caton, P. G. F., 1963: Wind Measurement by Doppler Radar. *Meteorological Magazine,* **92**, 213-222.

Cheng, M. D., 1989: Effects of Downdrafts and Mesoscale Convective Organization on the Heat and Moisture Budgets of Tropical Cloud Clusters. Part I: A Diagnostic Cumulus Ensemble Model. *J. Atmos. Sci.,* **46**, 1517-1538.

Cheng, M. D., and A. Arakawa, 1997: Inclusion of Rainwater Budget and Convective Downdrafts in the Arakawa-Schubert Cumulus Parameterization. *J. Atmos. Sci.,* **54**, 1359-1378.

Cohen, C., 2000: A Quantitative Investigation of Entrainment and Detrainment in Numerically Simulated Cumulonimbus Clouds. *J. Atmos. Sci.,* **57**, 1657-1674.

Conway, J. W., and D. S. Zrnic, 1993: A Study of Embryo Production and Hail Growth Using Dual-Doppler and Multiparameter Radars. *Mon. Wea. Rev.,* **121**, 2511-2528.

Doswell, C. A. III, 1985: *The Operational Meteorology of Convective Weather.* Volume II: *Storm Scale Analysis*. NOAA Tech. Mem. ERL ESG-15, U.S. Gov. Print. Off., 240 pp.

Emanuel, K. A., 1981: A Similarity Theory for Unsaturated Downdrafts within Clouds. *J. Atmos. Sci.,* **38**, 1541-1557.

Emanuel, K. A., 1986: Some Dynamical Aspects of Precipitating Convection. *J. Atmos. Sci.,* **43**, 2183-2198.

Emanuel, K. A., 1994: Atmospheric Convection. Oxford University Press, New York, NY, 580 pp.

Fujita, T. T., and H. R. Byers, 1977: Spearhead Echo and Downburst in the Crash of an Airliner. *Mon. Wea. Rev.,* **105**, 129-146.

Fujita, T. T., and R. M. Wakimoto, 1983: JAWS microbursts revealed by triple-Doppler radar, aircraft, and PAM data. Preprints, *13th Conf. Severe Local Storms,* Tulsa, Amer. Meteor. Soc., 97-100.

Gilmore, M. S., and L. J. Wicker, 1998: The Influence of Midtropospheric Dryness on Supercell Morphology and Evolution. *Mon. Wea. Rev.,* **126**, 943-958.

Holmes, D. W., and R. L. Smith, 1958: Doppler Radar for Weather Investigations. *7th Weather Radar Conference,* Proceedings, F-29-F-33.

Humphreys, W. J., 1914: The Thunderstorm and its phenomena. *Mon. Wea. Rev.,* **42**, 348-380.

Igau, R. C., M. A. LeMone, and D. Wei, 1999: Updraft and Downdraft Cores in TOGA COARE: Why So Many Buoyant Downdraft Cores? *J. Atmos. Sci.,* **56**, 2232-2245.

Johnson, R. H., 1976: The Role of Convective-Scale Precipitation Downdrafts in Cumulus and Synoptic-Scale Interactions. *J. Atmos. Sci.,* **33**, 1890-1910.

Kain, J. S., and J. M. Fritsch, 1990: A One-Dimensional Entraining/Detraining Plume Model and Its Application in Convective Parameterization. *J. Atmos. Sci.,* **47**, 2784-2802.

Kain, J. S., and J. M. Fritsch, 1993: Convective Parameterization for Mesoscale Models: The Kain-Fritsch Scheme. *The Representation of Cumulus Cconvection in Numerical Models.* Meteorological Monographs, No. 24, Amer. Meteor. Soc., 165-170.

Kessinger, C. J., D. B. Parsons, and J. W. Wilson, 1988: Observations of a Storm Containing Misocyclones, Downbursts, and Horizontal Vortex Circulations. *Mon. Wea. Rev.,* **116**, 1959-1982.

Kingsmill, D. E., and R. M. Wakimoto, 1991: Kinematic, Dynamic, and Thermodynamic Analysis of a Weakly Sheared Severe Thunderstorm over Northern Alabama. *Mon. Wea. Rev.,* **119**, 262-297.

Klemp, J. B., and R. B. Wilhelmson, 1978: The Simulation of Three-Dimensional Convective Storm Dynamics. *J. Atmos. Sci.,* **35**, 1070-1096.

Knupp, K. R., and W. R. Cotton: Convective Downdraft Structure: An Interpretive Survey. *Reviews of Geophysics,* **23**, 183-215.

Knupp, K. R., 1987: Downdrafts within High Plains Cumulonimbi. Part I: General Kinematic Structure. *J. Atmos. Sci.,* **44**, 987-1008.

Knupp, K. R., 1988: Downdrafts within High Plains Cumulonimbi. Part II: Dynamics and Thermodynamics. *J. Atmos. Sci.,* **45**, 3965-3982.

Knupp, K. R., 1996: Structure and Evolution of a Long-Lived, Microburst-Producing Storm. *Mon. Wea. Rev.,* **124**, 2785-2806.

Lhermitte, R. M., 1968: New Developments in Doppler Radar Methods. *13th Conference on Radar Meteorology,* Proceedings, 14-17.

Lhermitte, R. M., and M. Gilet, 1975: Dual-Doppler Radar Observation and Study of Sea Breeze Convective Storm Development. *J. Appl. Meteor.,* **14**, 1346-1361.

May, P. T., and D. K. Rajopadhyaya, 1999: Vertical Velocity Characteristics of Deep Convection over Darwin, Australia. *Mon. Wea. Rev.,* **127**, 1056-1071.

Miller, L. J., and W. Anderson, 1991: Multiple-Doppler Radar Wind Synthesis in CEDRIC. *Airborne Doppler Radar Data Analysis Workshop, 2000 NCAR Spring Colloquium, 8 pp.*

Moorthi, S., and M. J. Suarez, 1999: Documentation of Version 2 of Relaxed Arakawa-Schubert Cumulus Parameterization with Convective Downdrafts. *NOAA Technical Report NWS/NCEP 99-01,* 44 pp.

Ogura, Y., and T. Takahashi, 1971: Numerical Simulation of the Life Cycle of a Thunderstorm Cell. *Mon. Wea. Rev.,* **34**, 895-911.

Oye, R., and M. Case, 1995: REORDER: A Program for Gridding Radar Data. Installation and Use Manual for the Unix Version. *Airborne Doppler Radar Data Analysis Workshop, 2000 NCAR Spring Colloquium,* 24 pp.

Parsons, D. B., and M. L. Weisman, 1993: A Numerical Study of a Rotating Downburst. *J. Atmos. Sci.,* **50**, 2369-2385.

Proctor, F. H., 1988: Numerical Simulations of an Isolated Microburst. Part I: Dynamics and Structure. *J. Atmos. Sci.,* **45**, 3137-3160.

Proctor, F. H., 1989: Numerical Simulations of an Isolated Microburst. Part II: Sensitivity Experiments. *J. Atmos. Sci.,* **46**, 2143-2165.

Schmid, W., and H. H. Schiesser, 2000: The Origin of Severe Winds in a Tornadic Bow-Echo Storm over Northern Switzerland. *Mon. Wea. Rev.,* **128**, 192-207.

Seitter, K. L., and H. L. Kuo, 1983: The Dynamical Structure of Squall-Line Type Thunderstorms. *J. Atmos. Sci.,* **40**, 2831-2854.

Srivastava, R. C., 1985: A Simple Model of Evaporatively Driven Downdraft: Application to Microburst Downdraft. *J. Atmos. Sci.,* **42**, 1004-1023.

Srivastava, R. C., 1987: A Model of Intense Downdrafts Driven by the Melting and Evaporation of Precipitation. *J. Atmos. Sci.,* **44**, 1752-1773.

Sud, Y. C., and G. K. Walker, 1993: A Rain Evaporation and Downdraft Parameterization to Complement a Cumulus Updraft Scheme and Its Evaluation Using GATE Data. *Mon. Wea. Rev.,* **121**, 3019-3039.

Wakimoto, R. M., and V. N. Bringi, 1988: Dual-Polarization Observations of Microbursts Associated with Intense Convection: The 20 July Storm during the MIST Project. *Mon. Wea. Rev.,* **116**, 1521-1539.

Weisman, M. L., and J. B. Klemp, 1982: The Dependence of Numerically Simulated Convective Storms on Vertical Wind Shear and Buoyancy. *Mon. Wea. Rev.,* **110**, 504-520.